

Article

# Design and Performance of a New $\text{Zn}_{0.5}\text{Mg}_{0.5}\text{FeMnO}_4$ Porous Spinel as Anode Material for Li-Ion Batteries

Zakaria Chchiyai <sup>1</sup>, Oumayema El Ghali <sup>1</sup>, Abdelilah Lahmar <sup>2,\*</sup>, Jones Alami <sup>3</sup> and Bouchaib Manoun <sup>1,3</sup>

<sup>1</sup> Rayonnement-Matière et Instrumentation, S3M, FST, Hassan First University of Settat, Settat 26000, Morocco; chchiyai.zakaria@gmail.com (Z.C.); oumaimaelghali97@gmail.com (O.E.G.); bouchaib.manoun@um6p.ma (B.M.)

<sup>2</sup> Laboratoire de Physique de la Matière Condensée (LPMC), Université de Picardie Jules Verne, 33 rue Saint-Leu, 80039 Amiens, France

<sup>3</sup> Materials Science, Energy, and Nano-Engineering Department, University Mohammed VI Polytechnic, Ben Guerir 43150, Morocco; jones.alami@um6p.ma

\* Correspondence: abdel.ilah.lahmar@u-picardie.fr

**Abstract:** Due to the low capacity, low working potential, and lithium coating at fast charging rates of graphite material as an anode for Li-ion batteries (LIBs), it is necessary to develop novel anode materials for LIBs with higher capacity, excellent electrochemical stability, and good safety. Among different transition-metal oxides,  $\text{AB}_2\text{O}_4$  spinel oxides are promising anode materials for LIBs due to their high theoretical capacities, environmental friendliness, high abundance, and low cost. In this work, a novel, porous  $\text{Zn}_{0.5}\text{Mg}_{0.5}\text{FeMnO}_4$  spinel oxide was successfully prepared via the sol-gel method and then studied as an anode material for Li-ion batteries (LIBs). Its crystal structure, morphology, and electrochemical properties were, respectively, analyzed through X-ray diffraction, high-resolution scanning electron microscopy, and cyclic voltammetry/galvanostatic discharge/charge measurements. From the X-ray diffraction,  $\text{Zn}_{0.5}\text{Mg}_{0.5}\text{FeMnO}_4$  spinel oxide was found to crystallize in the cubic structure with  $Fd\bar{3}m$  symmetry. However, the  $\text{Zn}_{0.5}\text{Mg}_{0.5}\text{FeMnO}_4$  spinel oxide exhibited a porous morphology formed by interconnected 3D nanoparticles. The porous  $\text{Zn}_{0.5}\text{Mg}_{0.5}\text{FeMnO}_4$  anode showed good cycling stability in its capacity during the initial 40 cycles with a retention capacity of  $484.1 \text{ mAh g}^{-1}$  after 40 cycles at a current density of  $150 \text{ mA g}^{-1}$ , followed by a gradual decrease in the range of 40–80 cycles, which led to reaching a specific capacity close to  $300.0 \text{ mAh g}^{-1}$  after 80 cycles. The electrochemical reactions of the lithiation/delithiation processes and the lithium-ion storage mechanism are discussed and extracted from the cyclic voltammetry curves.

**Keywords:** porous  $\text{Zn}_{0.5}\text{Mg}_{0.5}\text{FeMnO}_4$  spinel; sol-gel route; crystallographic structure; Li-ion batteries; anode material; electrochemical performance



**Citation:** Chchiyai, Z.; El Ghali, O.; Lahmar, A.; Alami, J.; Manoun, B. Design and Performance of a New  $\text{Zn}_{0.5}\text{Mg}_{0.5}\text{FeMnO}_4$  Porous Spinel as Anode Material for Li-Ion Batteries. *Molecules* **2023**, *28*, 7010. <https://doi.org/10.3390/molecules28207010>

Academic Editor: Sheng-Heng Chung

Received: 8 August 2023

Revised: 23 September 2023

Accepted: 5 October 2023

Published: 10 October 2023



**Copyright:** © 2023 by the authors. Licensee MDPI, Basel, Switzerland. This article is an open access article distributed under the terms and conditions of the Creative Commons Attribution (CC BY) license (<https://creativecommons.org/licenses/by/4.0/>).

## 1. Introduction

Recently, the extensive demand for consumer electronics and electric vehicles has led to a significant increase in the demand for rechargeable lithium-ion batteries (LIBs) owing to their high energy density, long cycle life, environmental friendliness, and no memory effect [1–3]. Since the 1990s, LIBs have been regarded as one of the systems with the most energy storage and have gained widespread applications in mobile electronic devices such as handheld computers, tablets, and mobile phones. LIBs with higher energy density and fast-chargeable capability are requested for many energy storage systems, especially for electric vehicles (EV) and stationary energy storage devices [4–6].

In commercialized, traditional LIBs, graphite has been the most extensively used anode material to date due to its low cost and long cycle life [7,8]. Due to the low capacity of graphite material (only  $372 \text{ mAh g}^{-1}$ ), its low working potential ( $<0.2 \text{ V vs. Li}^+/\text{Li}$ ), and its lithium coating at fast charging rates, graphite-based LIBs are limited and cannot meet the demand for fast-chargeable batteries with high energy density [9,10]. Therefore,

developing novel anode materials for LIBs with higher capacity, low cost, nontoxicity, excellent electrochemical stability, and good safety has recently become an important research issue. In this regard, alloys and transition-metal oxides have appeared as the most popular possibilities to substitute the graphite material in LIBs [11–13].

In recent decades, transition-metal oxides (TMOs) with the general formula  $M_xO_y$  (where  $M = \text{Mn, Fe, Ni, Sn, Co, Cr, Zn, Nb, Mo, etc.}$ ) have received significant attention as promising high-performance anode materials to substitute the graphite material in LIBs due to their distinctive properties such as higher specific capacity than that of the commercially used graphite, good safety, environmental friendliness, and low price [14,15]. With respect to these characteristics, many TMOs have been widely studied as anode materials for LIBs, such as  $\text{MnO}$  [16],  $\text{NiO}$  [17],  $\text{CuO}$  [18],  $\text{TiO}_2$  [19],  $\text{MnO}_2$  [20],  $\text{SiO}_2$  [21],  $\text{Fe}_2\text{O}_3$  [22], and  $\text{SnO}_2$  [23]. Among these TMOs,  $\text{AB}_2\text{O}_4$ -type spinels as mixed transition-metal oxides with a greater capacity than graphite anodes ( $800\text{--}1000 \text{ mAh g}^{-1}$ ) have received a lot of attention; they are considered interesting and promising electrochemically active materials for next-generation LIBs, which can combine two transition metals [24,25]. Generally,  $\text{AB}_2\text{O}_4$  spinel oxides as anode materials for LIBs use the conversion mechanism for  $\text{Li}^+$  ion storage [26]. In general,  $\text{AB}_2\text{O}_4$ -type spinel oxides with the desired morphology can be easily synthesized through several methods such as solid-state reaction [27], sol-gel [28], co-precipitation [29], hydrothermal [30], electrospinning [31], low-temperature solution combustion [32], microwave-induced combustion [33], and Pechini [34] methods, among others. In recent years, many types of spinel ferrite have been used and emerged as conversion anode materials for LIBs, such as ferrite  $\text{Fe}_3\text{O}_4$  [35], copper ferrite  $\text{CuFe}_2\text{O}_4$  [36], cobalt ferrite  $\text{CoFe}_2\text{O}_4$  [37], nickel ferrite  $\text{NiFe}_2\text{O}_4$  [38], etc.

Recently, nanostructured spinel ferrites have received tremendous interest for application in LIBs [39]. Among nanostructured spinel ferrites, magnesium ferrite  $\text{MgFe}_2\text{O}_4$  nanoparticles prepared through the sol-gel method, as anode materials for LIBs, have shown a specific capacity near  $474 \text{ mAh g}^{-1}$  after 50 cycles under a current density of  $90 \text{ mA g}^{-1}$  [40]. In this phase, Mg was used as an electrochemical inactive pillar to enhance the cyclability of  $\text{MgFe}_2\text{O}_4$  spinel [30]. The manganese ferrite  $\text{MnFe}_2\text{O}_4$  with mesoporous microsphere morphology has been reported by Z. Zhang et al. [41]. It has shown specific capacities of  $712.2$  and  $552.2 \text{ mA h g}^{-1}$  at  $0.2 \text{ C}$  and  $0.8 \text{ C}$ , respectively, after 50 cycles, suggesting good performance for fast charging. Another spinel ferrite, zinc ferrite  $\text{ZnFe}_2\text{O}_4$ , has gained much attention as an anode material for LIBs due to its great electrochemical performance with different morphologies, such as hollow spherical [42], microsized capsules [43], macroporous [44], porous nanospheres [45], and fiber-in-tube [46] morphologies, among others.

Additionally, manganese-based  $\text{AB}_2\text{O}_4$  spinel oxides have also attracted much interest as alternative electrode materials for LIBs owing to their excellent electrochemical performance [47,48]. Among these manganites,  $\text{ZnMn}_2\text{O}_4$  microspheres were synthesized by K. Cai et al. using a microwave-assisted hydrothermal route [49]. From their electrochemical properties, they showed a capacity of  $337.3 \text{ mAh g}^{-1}$  after 40 cycles at a rate of  $0.1 \text{ C}$ . Another spinel manganite, the  $\text{MgMn}_2\text{O}_4$  spinel, was investigated by Z. Wang et al. [50]. The  $\text{MgMn}_2\text{O}_4$  nanoparticles with particle sizes ranging from  $20$  to  $30 \text{ nm}$  prepared using the sol-gel method have shown a discharge capacity of  $483.6 \text{ mAh g}^{-1}$  after 100 cycles.

In recent years, Co-, Ni-, Zn-, Fe-, Cr-, Mn-, and Li-based multi-component spinel oxides have attracted great attention as high-performance anodes for LIBs and long-life lithium-ion batteries [51,52]. L. Dong et al. [51] reported a multi-component transition-metal oxide  $(\text{Ni,Co,Mn})\text{Fe}_2\text{O}_{4-x}$  with oxygen vacancies as an anode material for LIBs, which has shown a specific capacity of  $650.5 \text{ mAh g}^{-1}$  at  $2 \text{ A g}^{-1}$  after 1200 cycles, i.e., excellent reversible capacity and good cycling stability. K. Tian et al. [52] found that spinel oxides  $(\text{CoNiZnXMnLi})_3\text{O}_4$  ( $X = \text{Fe, Cr}$ ) are high-performance anodes for LIBs. On the other hand, Nb-based oxides such as  $\text{Nb}_2\text{O}_5$ ,  $\text{Nb}_{12}\text{O}_{29}$ ,  $\text{TiNb}_2\text{O}_7$ ,  $\text{Ti}_2\text{Nb}_{10}\text{O}_{29}$ , etc., have attracted much attention as anode materials for high-rate lithium-ion energy storage [53].

From the above, to simultaneously improve the stability, energy density, and high-rate capability of anode materials for LIBs, a novel, 3D interconnected structure belonging to transition-metal-oxide-type spinels is urgently needed. In this work, we report a facile route to synthesize 3D porous  $\text{Zn}_{0.5}\text{Mg}_{0.5}\text{FeMnO}_4$  spinel oxide using sol-gel method with a theoretical capacity of  $976.3 \text{ mAh g}^{-1}$  as an anode electrode for LIBs. Herein, Mg is used as an inactive stabilized pillar, which can produce good cycling stability. The synthesized active material is characterized by different techniques such as X-ray diffraction, thermogravimetry analysis, scanning electron microscopy, and the nitrogen adsorption-desorption isotherm to report, respectively, its crystallographic structure, thermal stability, morphology, and specific surface area. The electrochemical performance of the prepared porous  $\text{Zn}_{0.5}\text{Mg}_{0.5}\text{FeMnO}_4$  spinel oxide is tested by cyclic voltammetry and galvanostatic discharge/charge measurements.

## 2. Results and Discussion

### 2.1. X-ray Diffraction, Rietveld Refinement, and Crystal Structure

The X-ray powder diffraction (XRD) technique was first employed to analyze the crystallographic structure, formation, and phase purity of the as-synthesized  $\text{Zn}_{0.5}\text{Mg}_{0.5}\text{FeMnO}_4$  sample. Figure 1a shows the wide-angle XRD pattern of the  $\text{Zn}_{0.5}\text{Mg}_{0.5}\text{FeMnO}_4$  sample acquired at room temperature. From this figure, the XRD data reveal the formation of the  $\text{AB}_2\text{O}_4$ -type spinel phase as all the experimental XRD peaks observed at different  $2\theta$  values are well matching with standard peaks of the  $\text{MgFe}_2\text{O}_4$  spinel phase that crystallizes in the cubic  $Fd\bar{3}m$  structure with a lattice parameter of  $a = 8.3827 \text{ \AA}$  (JCPDS card: 88-1936) [54], which indicates that the as-synthesized  $\text{Zn}_{0.5}\text{Mg}_{0.5}\text{FeMnO}_4$  sample exhibits a single spinel phase with the cubic  $Fd\bar{3}m$  system. However, no additional peaks from any impurities could be identified in the XRD pattern, revealing a high purity of the synthesized spinel phase and confirming that the organic species of CA have been completely removed. In addition, the synthesized spinel shows sharp XRD peaks with small full width at half maximum (FWHM), suggesting good crystallization of the synthesized  $\text{Zn}_{0.5}\text{Mg}_{0.5}\text{FeMnO}_4$  spinel oxide. Besides, the widening of the obtained XRD peaks provides proof of the existence of nanoscale-dimension spinel particles.

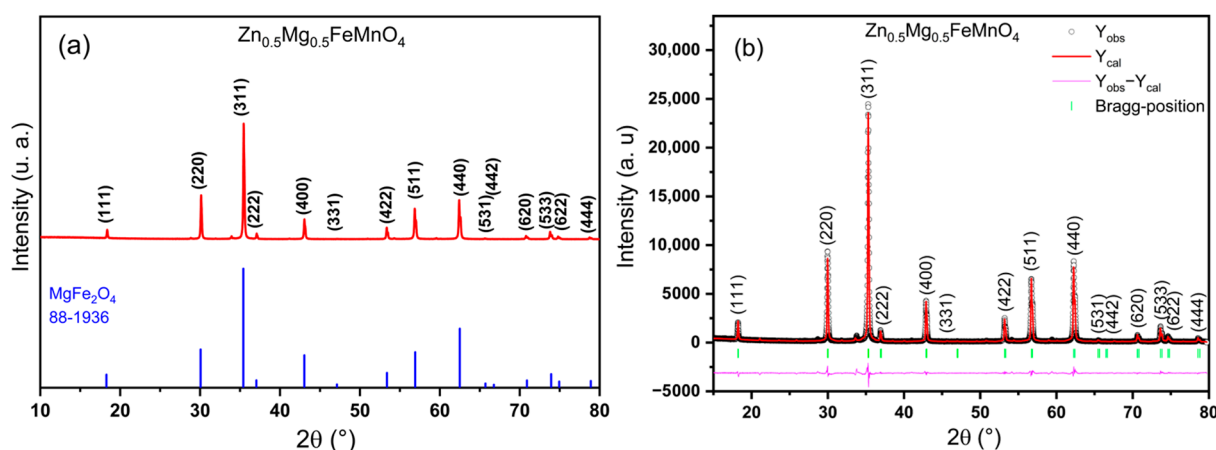


**Figure 1.** (a) X-ray powder diffraction pattern of the elaborated  $\text{Zn}_{0.5}\text{Mg}_{0.5}\text{FeMnO}_4$  spinel oxide compared with JCPDS card no. 88-1936 of the  $\text{MgFe}_2\text{O}_4$  phase. (b) Rietveld refinement of the XRD pattern for the elaborated  $\text{Zn}_{0.5}\text{Mg}_{0.5}\text{FeMnO}_4$  spinel oxide with the cubic  $Fd\bar{3}m$  structure.

For further deep analysis of structural parameters, the XRD pattern of the synthesized  $\text{Zn}_{0.5}\text{Mg}_{0.5}\text{FeMnO}_4$  spinel ferrite was refined using the Rietveld method [55,56]. The structural refinement was carried out with the cubic structure and  $Fd\bar{3}m$  as a space group. The Rietveld refinement plot of the synthesized  $\text{Zn}_{0.5}\text{Mg}_{0.5}\text{FeMnO}_4$  spinel is displayed in Figure 1b, where the Bragg reflections are revealed by the green vertical bars, the observed

XRD ( $Y_{\text{obs}}$ ) pattern is shown by open black circles, the simulated XRD ( $Y_{\text{cal}}$ ) pattern by the Rietveld method is represented by red solid lines, and the difference curve ( $Y_{\text{obs}} - Y_{\text{cal}}$ ) is indicated by pink solid lines. From this figure, it can be seen that the observed XRD pattern shows great agreement with the calculated XRD pattern, revealing the success of a realized structural refinement for the synthesized  $\text{Zn}_{0.5}\text{Mg}_{0.5}\text{FeMnO}_4$  spinel ferrite. Moreover, the quality of the structural refinement was evaluated by the consideration of the different R-factors such as structure factor ( $R_{\text{F}}$ ), Bragg factor ( $R_{\text{B}}$ ), profile factor ( $R_{\text{P}}$ ), expected factor ( $R_{\text{exp}}$ ), and profile factor ( $R_{\text{wp}}$ ) [57–60]. The results of the powder X-ray diffraction of the synthesized  $\text{Zn}_{0.5}\text{Mg}_{0.5}\text{FeMnO}_4$  spinel oxide in the Rietveld refinement such as structural parameters, profile parameters, and different reliability R-factors are summarized in Table 1. According to the obtained values of different R-factors, the synthesized  $\text{Zn}_{0.5}\text{Mg}_{0.5}\text{FeMnO}_4$  spinel oxide crystallizes in the cubic  $Fd\bar{3}m$  structure with a lattice parameter of  $a = 8.4265(2) \text{ \AA}$ .

**Table 1.** The results of the Rietveld structural refinement for structural parameters, profile parameters, and various reliability R-factors of the elaborated  $\text{Zn}_{0.5}\text{Mg}_{0.5}\text{FeMnO}_4$  spinel oxide.

Wavelengths ( $\text{\AA}$ )	Lattice Parameters	Crystal Structure	Mixing Factor	Caglioti Parameters	R-Factors
$\lambda_{k\alpha 1} = 1.54056$ $\lambda_{k\alpha 2} = 1.54439$	$a = 8.4265(2) \text{ \AA}$ $V = 598.33(1) \text{ \AA}^3$	Cubic $Fd\bar{3}m$	$\eta = 635(7)$	$U = 0.029(6)$ $V = -0.011(6)$ $W = 0.0154(2)$	$R_{\text{F}} = 2.41, R_{\text{B}} = 2.83$ $R_{\text{P}} = 7.27, R_{\text{exp}} = 11.5$ $R_{\text{wp}} = 12.3$

From the obtained structural parameters by Rietveld refinement, the crystal structure of  $\text{Zn}_{0.5}\text{Mg}_{0.5}\text{FeMnO}_4$  spinel oxide was drawn. Figure 2 displays the crystal structure of  $\text{Zn}_{0.5}\text{Mg}_{0.5}\text{FeMnO}_4$  spinel oxide with the cubic structure in  $Fd\bar{3}m$  symmetry. As clearly shown in the figure, the crystal structure of  $\text{Zn}_{0.5}\text{Mg}_{0.5}\text{FeMnO}_4$  spinel oxide is constructed by 3D interconnected tetrahedral and octahedral polyhedra, where  $\text{Zn}^{2+}$  and  $\text{Mg}^{2+}$  cations are located in the tetrahedral sites (green balls),  $\text{Fe}^{3+}$  and  $\text{Mn}^{3+}$  are located in the octahedral sites (blue balls), and the red balls represent the  $\text{O}^{2-}$  oxygen anions. Moreover, this structure shows three Wyckoff sites—the 8a, 16d, and 32e sites, which correspond to the tetrahedral, octahedral, and oxygen sites, respectively. Only 1/8 of the tetrahedral sites are occupied by  $\text{Zn}^{2+}/\text{Mg}^{2+}$  cations, 1/2 of the octahedral sites are occupied by  $\text{Fe}^{3+}/\text{Mn}^{3+}$  cations, and the 32e sites are totally occupied by oxygen anions. Therefore, the spinel structure exhibits 7/8 of the tetrahedral sites and 1/2 of the octahedral sites that are empty. During the first discharge of electrochemical cells, the lithium ions can be inserted into the unit cell to occupy the lacunar sites.

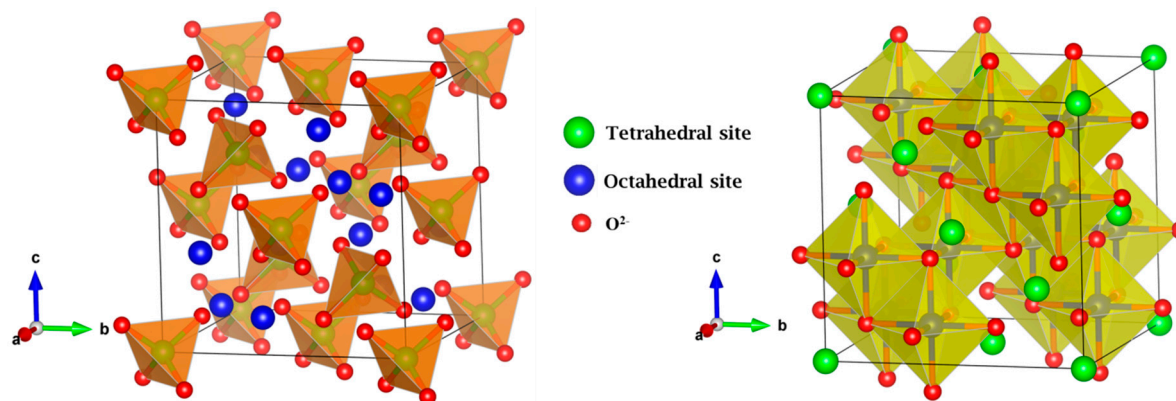


**Figure 2.** Three-dimensional crystal structure of  $\text{Zn}_{0.5}\text{Mg}_{0.5}\text{FeMnO}_4$  spinel oxide with the cubic  $Fd\bar{3}m$  structure. The  $\text{Zn}^{2+}$  and  $\text{Mg}^{2+}$  cations are located in the tetrahedral sites (green balls),  $\text{Fe}^{3+}$  and  $\text{Mn}^{3+}$  cations are located in the octahedral sites (blue balls), and the red balls represent the  $\text{O}^{2-}$  oxygen anions.

## 2.2. Thermal Analysis

In order to understand the mechanism of the calcination of the synthesized xerogel, the xerogel sample was characterized by thermogravimetric analysis (TGA) in a wide temperature range of 20–700 °C. Figure 3 depicts the thermogravimetric curves (TG) of the synthesized xerogel and the calcined sample of  $\text{Zn}_{0.5}\text{Mg}_{0.5}\text{FeMnO}_4$  spinel. In the case of the xerogel sample (red curve), two weight losses take place in the temperature range from room temperature to 350 °C. The first loss is observed before 140 °C, which is due to the evaporation of the water used as a solvent during the synthesis and the physically adsorbed water on the surface. The second weight loss observed in the temperature range of 140–350 °C is attributed to the decomposition of the organic species of the citric acid (CA) associated with the elimination of nitrogen dioxide ( $\text{NO}_2$ ). Further, no weight loss is present above 350 °C. Moreover, the thermal stability of the synthesized spinel was examined by thermogravimetric analysis (TGA). For the calcined sample at 700 °C (blue curve), its TG curve demonstrates no weight loss in the whole temperature range of 20–700 °C, indicating good thermal stability of the synthesized porous  $\text{Zn}_{0.5}\text{Mg}_{0.5}\text{FeMnO}_4$  spinel oxide and confirming that the organic molecules of the citric acid (CA) have been completely removed after calcination at 700 °C.

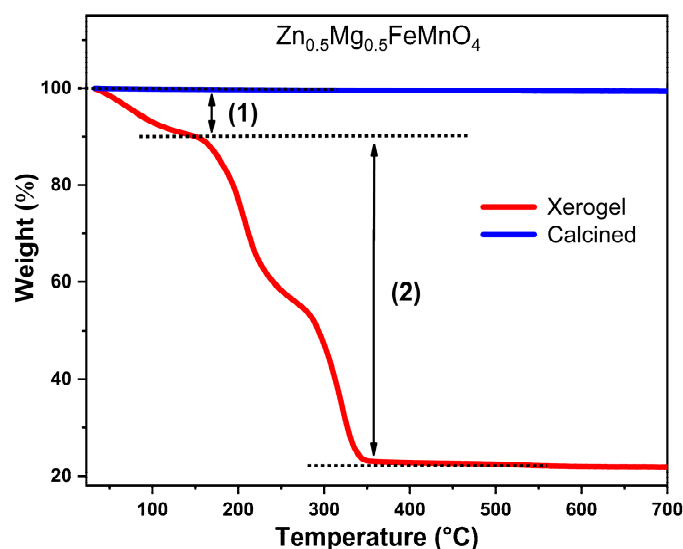


**Figure 3.** Thermogravimetric curves (TG) of the synthesized xerogel and calcined sample of  $\text{Zn}_{0.5}\text{Mg}_{0.5}\text{FeMnO}_4$  spinel.

## 2.3. Morphology, Purity, and Specific Surface

The microstructural morphology of the synthesized spinel was revealed by scanning electron microscopy (SEM). Figure 4a shows the SEM image of the synthesized  $\text{Zn}_{0.5}\text{Mg}_{0.5}\text{FeMnO}_4$  spinel oxide, which demonstrates its surface morphology. From the figure, it can be seen that the prepared spinel shows a micro-sized porous morphology with different pore sizes ranging from 2 to 5  $\mu\text{m}$ . Moreover, the porous morphology can make the electrolyte used in the cells of LIBs penetrate easily, which leads to the acceleration of lithium ions diffusion, enhancing the electrochemical performance. For further deep analysis of the surface morphology, the synthesized spinel was characterized by high-resolution scanning electron microscopy (HR-SEM). The obtained HR-SEM image is presented in Figure 4b. It can be seen from this figure that the porous  $\text{Zn}_{0.5}\text{Mg}_{0.5}\text{FeMnO}_4$  spinel is composed of interconnected nanosized spherical particles with sizes ranging from 50 to 100 nm.

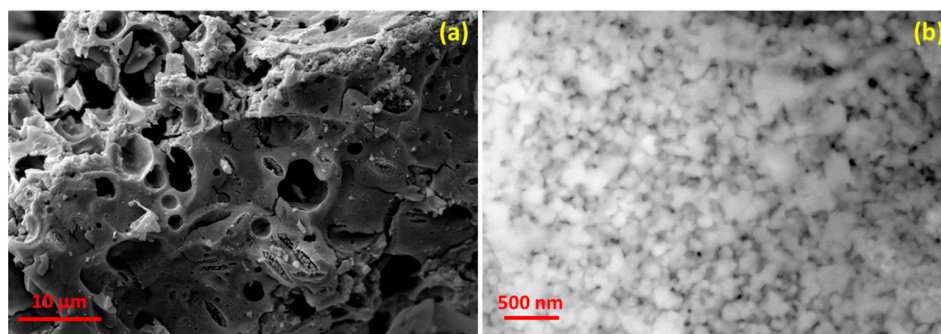


**Figure 4.** (a) Scanning electron microscopy (SEM) image of the synthesized porous  $\text{Zn}_{0.5}\text{Mg}_{0.5}\text{FeMnO}_4$  spinel oxide and (b) its high-resolution scanning electron microscopy (HR-SEM) image.

To carry out an investigation on the purity of the synthesized porous  $\text{Zn}_{0.5}\text{Mg}_{0.5}\text{FeMnO}_4$  spinel oxide, an energy-dispersive X-ray (EDX) spectrometer was utilized. The results of this investigation are displayed in Figure 5. As clearly shown in the figure, only Zn, Mg, Fe, Mn, and O peaks could be recorded, which suggests the existence of only Zn, Mg, Fe, Mn, and O elements in the product. No additional element was recorded. The EDX results confirm approximately the atomic ratio 0.5:0.5:1:1:4 of Zn, Mg, Fe, Mn, and O elements, respectively, which gives further proof of the high purity of the synthesized spinel. Besides, the SEM/EDX instrument was also used to provide different element distribution maps of the 3D metal oxide network. The surface of the synthesized spinel and its EDX element mapping results are shown in Figure 6. From these maps, it is clearly demonstrated that the Zn, Mg, Fe, Mn, and O elements are uniformly distributed across the whole sample.

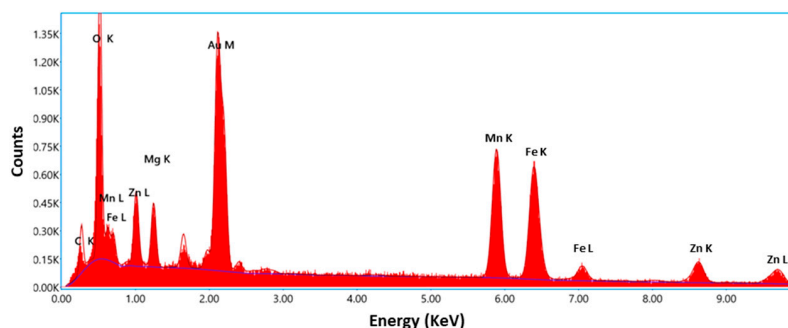


**Figure 5.** EDX spectrum of the synthesized porous  $\text{Zn}_{0.5}\text{Mg}_{0.5}\text{FeMnO}_4$  spinel oxide.

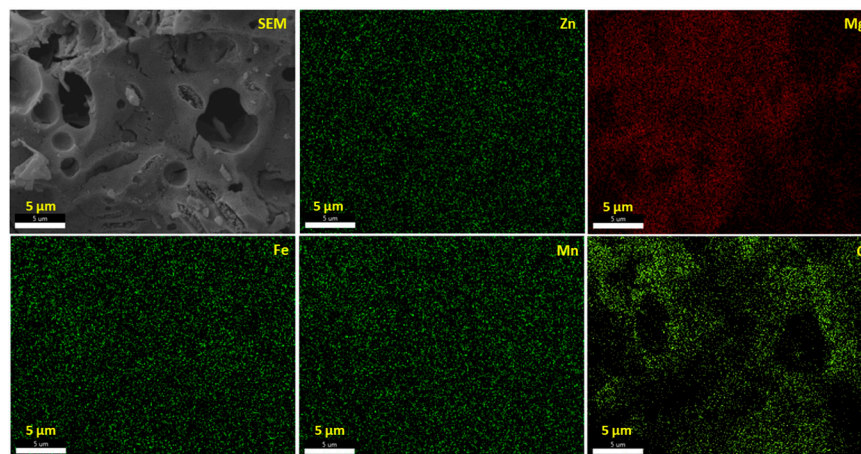


**Figure 6.** The SEM image and EDX element mapping results of Zn, Mg, Fe, Mn, and O of the synthesized porous  $\text{Zn}_{0.5}\text{Mg}_{0.5}\text{FeMnO}_4$  spinel oxide. Scale bar, 5  $\mu\text{m}$ .

Figure 7 shows the nitrogen adsorption–desorption isotherm of the synthesized porous  $\text{Zn}_{0.5}\text{Mg}_{0.5}\text{FeMnO}_4$  spinel oxide collected at a liquid nitrogen temperature of 77 K. The analysis of the nitrogen adsorption–desorption isotherm was performed to obtain the specific surface area of the synthesized porous  $\text{Zn}_{0.5}\text{Mg}_{0.5}\text{FeMnO}_4$  spinel oxide using the Brunauer–Emmett–Teller (BET) method. From the nitrogen adsorption–desorption isotherm, the porous spinel shows a type IV nitrogen sorption isotherm with a small hysteresis loop at high partial pressures ( $P/P_0$ ), suggesting a characteristic of a mesoporous material. Using the Brunauer–Emmett–Teller (BET) method, the specific surface area of the synthesized porous  $\text{Zn}_{0.5}\text{Mg}_{0.5}\text{FeMnO}_4$  spinel oxide was found to be  $13.54 \text{ m}^2 \text{ g}^{-1}$ . The obtained small specific surface area is probably due to the high aggregation of nanoparticles, as shown in the HR-SEM image (Figure 4b). Moreover, the synthesized porous  $\text{Zn}_{0.5}\text{Mg}_{0.5}\text{FeMnO}_4$  spinel oxide has a larger specific surface area than that of graphite powder, which is  $6.89 \text{ m}^2 \text{ g}^{-1}$  [61].

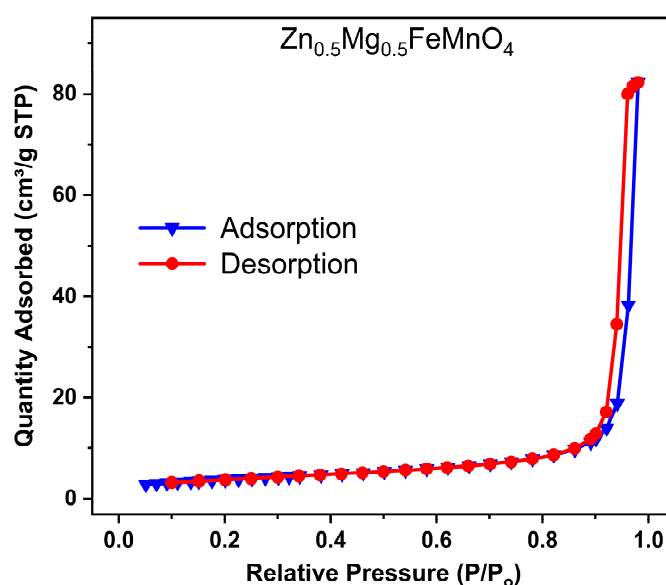
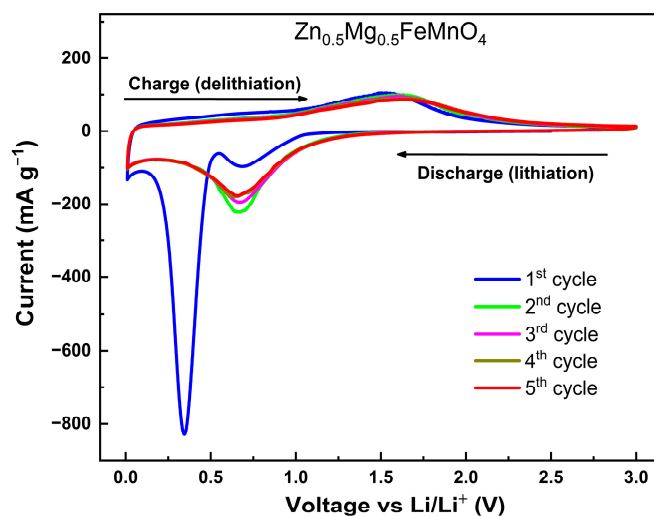


Figure 7. Nitrogen adsorption–desorption isotherm of the synthesized porous  $\text{Zn}_{0.5}\text{Mg}_{0.5}\text{FeMnO}_4$  spinel oxide.

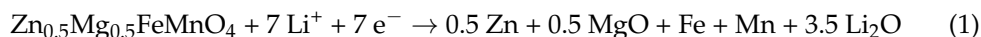
#### 2.4. Electrochemical Results

In order to further investigate the beneficial effects of the  $\text{Zn}_{0.5}\text{Mg}_{0.5}\text{FeMnO}_4$  spinel oxide with a porous morphology as anode for LIBs, its electrochemical performance was analyzed in a half-cell configuration. The cyclic voltammetry (CV) measurements were conducted over the 0.01–3.00 V voltage range vs.  $\text{Li}^+/\text{Li}$  under ambient conditions. Figure 8 shows the initial five CV curves of the synthesized porous  $\text{Zn}_{0.5}\text{Mg}_{0.5}\text{FeMnO}_4$  spinel oxide collected at a sweep rate of  $0.05 \text{ mV s}^{-1}$ . Specifically, in the initial cathodic sweep (discharge, lithiation), two dominant peaks at 0.35 and 0.7 V are observed in the first cycle. In agreement with previous studies [62,63], the cathodic peak that appeared at 0.7 V is attributed to the reversible reduction of  $\text{Zn}^{2+}$ ,  $\text{Fe}^{3+}$ , and  $\text{Mn}^{3+}$  ions together, which are incorporated in  $\text{Zn}_{0.5}\text{Mg}_{0.5}\text{FeMnO}_4$  spinel phase to their metallic states Zn, Fe, and Mn associated with the formation of MgO and amorphous  $\text{Li}_2\text{O}$ , as demonstrated in Equation (1). After the reduction of  $\text{Zn}_{0.5}\text{Mg}_{0.5}\text{FeMnO}_4$ , the formed Zn metal can react with  $\text{Li}^+$  ions, giving the reversible formation of LiZn alloys (Equation (2)) [46]. The other intense peak observed at 0.35 V corresponds to electrolyte decomposition, which leads to the irreversible formation of a solid electrolyte interface (SEI) [64,65]. For the subsequent cathodic sweeps, only one peak is obtained near 0.67 V, which is assigned to the reduction of ZnO,  $\text{Fe}_2\text{O}_3$ , and MnO to Zn, Fe, and Mn, respectively, as previously reported [66,67]. The electrochemical reactions of the lithiation process (discharge) can be shown, as reported in [68,69].

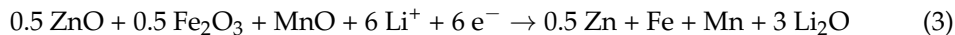


**Figure 8.** Cyclic voltammetry (CV) curves of the synthesized porous  $\text{Zn}_{0.5}\text{Mg}_{0.5}\text{FeMnO}_4$  spinel oxide measured over the 0.01–3.00 V voltage range (vs.  $\text{Li}^+/\text{Li}$ ) at a scan rate of  $0.05 \text{ mV s}^{-1}$  for the initial five cycles.

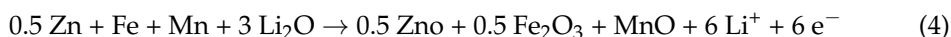
- First cycle:



- Subsequent cycles:



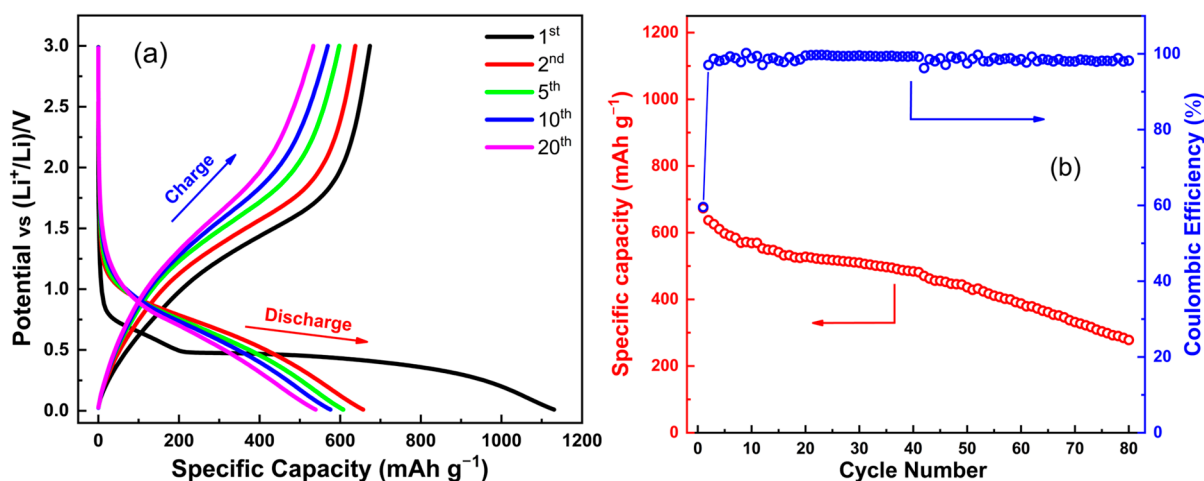
In the charge process (delithiation), the distinct anodic peaks are between 1.6 V and 1.8 V for all cycles, which probably contribute to the various oxidations of metallic Zn, Fe, and Mn to their oxide states  $\text{Zn}^{2+}$  (ZnO),  $\text{Fe}^{3+}$  ( $\text{Fe}_2\text{O}_3$ ), and  $\text{Mn}^{2+}$  (MnO), respectively, as represented in Equation (4) [39,70]. Therefore, the related reactions of the charge process (delithiation) for all cycles can be summarized as follows [71,72]:



On the other hand, the first cycle is easily distinct from the subsequent cycles. Besides, the difference between the redox peaks in the first and subsequent cycles is due to the capacity loss of the anode spinel during the first cycle. From the third cycle, the CV curves are similar and the redox peaks remain consistent, revealing good reversibility of the  $\text{Zn}_{0.5}\text{Mg}_{0.5}\text{FeMnO}_4$  anode.

Subsequently, the results of the galvanostatic discharge/charge cycling of the synthesized porous  $\text{Zn}_{0.5}\text{Mg}_{0.5}\text{FeMnO}_4$  spinel oxide acquired at a current density of  $150 \text{ mA g}^{-1}$  over the potential region of 0.01–3.00 V (vs.  $\text{Li}^+/\text{Li}$ ) for various cycles (1st, 2nd, 5th, 10th, and 20th) are shown in Figure 9a. In accordance with previous reports, the profile of the potential versus capacity plot of the studied porous  $\text{Zn}_{0.5}\text{Mg}_{0.5}\text{FeMnO}_4$  spinel oxide is similar to those of  $\text{ZnFe}_2\text{O}_4$  and  $\text{MgFe}_2\text{O}_4$  [73]. It is worth recalling that the  $\text{Zn}_{0.5}\text{Mg}_{0.5}\text{FeMnO}_4$  spinel oxide has a theoretical capacity of  $976.3 \text{ mAh g}^{-1}$  as an anode electrode for LIBs. From Figure 9a, the initial discharge and charge capacities are  $1132.9$  and  $676.4 \text{ mA h g}^{-1}$ , respectively. Note that the initial discharge capacity is higher than the theoretical capacity. This can be explained by the lithium-ion storage through a surface faradic redox reaction (pseudocapacitive). The irreversible capacity loss between discharge and charge of the first cycle is normally due to the formation of SEI film [74,75]. The studied

spinel displays an extended voltage plateau at about 0.5 V followed by a gradual slope for the first discharge. The potential plateau is probably due to the conversion from the reduction of  $\text{Zn}^{2+}$ ,  $\text{Fe}^{3+}$ , and  $\text{Mn}^{3+}$  transition metals to metallic states of Zn, Fe, and Mn, respectively [76,77]. During discharge/charge cycling, the discharge and charge capacities gradually decrease with increasing cycle numbers, which is probably attributed to the aggregation and pulverization of  $\text{Zn}_{0.5}\text{Mg}_{0.5}\text{FeMnO}_4$  nanoparticles, leading to poor electrical contacts between  $\text{Zn}_{0.5}\text{Mg}_{0.5}\text{FeMnO}_4$  nanoparticles and that between the active material and current collector [40]. The cycling performance of the  $\text{Zn}_{0.5}\text{Mg}_{0.5}\text{FeMnO}_4$  anode at the current density of  $150 \text{ mA g}^{-1}$  during 80 cycles is displayed in Figure 9b. It is clearly seen that the  $\text{Zn}_{0.5}\text{Mg}_{0.5}\text{FeMnO}_4$  anode shows good cycling stability in its capacity during the initial 40 cycles, with a specific capacity of  $484.1 \text{ mAh g}^{-1}$  after 40 cycles followed by a gradual decrease in the range of 40–80 cycles. Moreover, the  $\text{Zn}_{0.5}\text{Mg}_{0.5}\text{FeMnO}_4$  anode exhibits a specific capacity close to  $300.0 \text{ mAh g}^{-1}$  after 80 cycles at an applied current density of  $150 \text{ mA g}^{-1}$ . For the first cycle, the anode gives a Coulombic efficiency of 60.2%, which is owing to the abovementioned capacity loss in the first cycle. From the second cycle, the anode provides a stable value of Coulombic efficiency, which is more than 98% during 80 cycles. In order to compare the obtained performance with the literature, Table 2 compares the results of the electrochemical performance of the elaborated  $\text{Zn}_{0.5}\text{Mg}_{0.5}\text{FeMnO}_4$  spinel oxide with previously studied anodes.

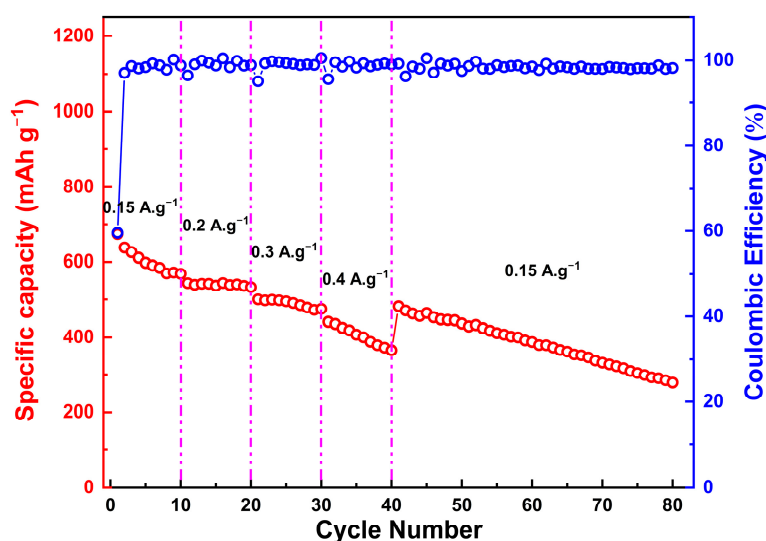


**Figure 9.** Electrochemical analyses of the synthesized porous  $\text{Zn}_{0.5}\text{Mg}_{0.5}\text{FeMnO}_4$  spinel oxide: (a) selected galvanostatic discharge/charge curves measured over the 0.01–3.00 V voltage range (vs.  $\text{Li}^+/\text{Li}$ ) at an applied current density of  $0.15 \text{ A g}^{-1}$  for various cycles (1st, 2nd, 5th, 10th, and 20th) and (b) cycling stability in its specific capacity and Coulombic efficiency during 80 cycles.

As presented in Figure 10, the rate performance of the studied  $\text{Zn}_{0.5}\text{Mg}_{0.5}\text{FeMnO}_4$  anode is examined by increasing the scan rates from  $150$  to  $400 \text{ mA g}^{-1}$  and then back to  $150 \text{ mA g}^{-1}$ . For the first current density ( $150 \text{ mA g}^{-1}$ ), the  $\text{Zn}_{0.5}\text{Mg}_{0.5}\text{FeMnO}_4$  anode reaches a specific capacity of  $569.1 \text{ mAh g}^{-1}$  after 10 cycles. When gradually increasing the current density, the specific capacity of the  $\text{Zn}_{0.5}\text{Mg}_{0.5}\text{FeMnO}_4$  anode gradually decreases and reaches a specific capacity of  $533.2 \text{ mAh g}^{-1}$  after 20 cycles at a current density of  $200 \text{ mA g}^{-1}$ , and a specific capacity of  $474.6 \text{ mAh g}^{-1}$  after 30 cycles at a current density of  $300 \text{ mA g}^{-1}$ , with good cycling stability. For the subsequent 10 cycles, the  $\text{Zn}_{0.5}\text{Mg}_{0.5}\text{FeMnO}_4$  anode exhibits a specific capacity of  $365.3 \text{ mAh g}^{-1}$  after 40 cycles at a current density of  $400 \text{ mA g}^{-1}$ . When the current density is switched back to  $150 \text{ mA g}^{-1}$ , the specific capacity of the studied anode increased rapidly to reach  $481.8 \text{ mAh g}^{-1}$ . In the range of 40–80 cycles, the  $\text{Zn}_{0.5}\text{Mg}_{0.5}\text{FeMnO}_4$  anode was found to show a gradual decrease during discharge/charge cycling and reached a specific capacity close to  $300.0 \text{ mAh g}^{-1}$  after 80 cycles at an applied current density of  $150 \text{ mA g}^{-1}$ .

**Table 2.** The results of the electrochemical performance of the elaborated  $\text{Zn}_{0.5}\text{Mg}_{0.5}\text{FeMnO}_4$  spinel oxide compared with previously studied anodes.

Anode	Applied Current Density ( $\text{mA g}^{-1}$ )	Cycle Number	Specific Capacity ( $\text{mAh g}^{-1}$ )	Ref.
Graphite	76	50	265	[78]
$\text{MgFe}_2\text{O}_4$ nanoparticles	90	50	474	[40]
$\text{MnFe}_2\text{O}_4$ mesoporous microspheres	744	50	552	[41]
$\text{ZnFe}_2\text{O}_4$ porous nanospheres	200	80	869	[45]
$\text{ZnMn}_2\text{O}_4$ microsheets	90	40	337	[49]
$\text{MgMn}_2\text{O}_4$ nanoparticles	50	100	484	[50]
Porous $\text{Zn}_{0.5}\text{Mg}_{0.5}\text{FeMnO}_4$	150	80	300	This work

**Figure 10.** Rate performance analysis of the synthesized porous  $\text{Zn}_{0.5}\text{Mg}_{0.5}\text{FeMnO}_4$  spinel oxide measured over the 0.01–3.00 V voltage range (vs.  $\text{Li}^+/\text{Li}$ ) with step-wise increasing current rates of 0.15, 0.2, 0.3, and 0.4  $\text{A g}^{-1}$ .

For further deep analysis of the kinetics of electrochemical lithiation/delithiation processes, the CV curves of the studied  $\text{Zn}_{0.5}\text{Mg}_{0.5}\text{FeMnO}_4$  anode were acquired at various scan rates ranging from 0.05 to 0.40  $\text{mV s}^{-1}$ , as shown in Figure 11a. The measured peak current ( $i$ ) for the cathodic and anodic sweeps at various scan rates ( $v$ ) was used to analyze the lithium-ion intercalation kinetics of the studied  $\text{Zn}_{0.5}\text{Mg}_{0.5}\text{FeMnO}_4$  anode. For the cathodic and anodic sweeps, the peak current ( $i$ , A) and the scan rates ( $v$ ,  $\text{mV s}^{-1}$ ) can be related according to the Dunn relation, as expressed in Equation (6) [79,80]:

$$i = av^b \quad (6)$$

Both sides of Equation (6) were taken in the logarithm function, which can be written as

$$\text{Log}(i) = \text{Log}(a) + b \text{Log}(v) \quad (7)$$

In these expressions,  $a$  and  $b$  are adjustable parameters. In general, three lithium-ion intercalation kinetics can be distinguished depending on the  $b$ -value. In particular, when the  $b$ -value approaches 0.5, the lithium-ion storage mechanism is controlled by the diffusion process. When the  $b$ -value is close to 1, the lithium-ion storage mechanism is through a surface faradic redox reaction (pseudocapacitive); whereas, when the  $b$ -value is between 0.5 and 1, the lithium-ion storage mechanism is a combination of a pseudocapacitive process and diffusion-controlled insertion [81]. The  $b$ -value was determined by plotting

$\text{Log}(i)$  against  $\text{Log}(v)$  for cathodic and anodic peaks, as shown in Figure 11b. The  $b$ -value for the cathodic and anodic sweeps corresponds to the slope of linear fitting of the peak currents versus scan rates. According to the estimated slopes (Figure 11b), the lithium-ion storage mechanism of the studied  $\text{Zn}_{0.5}\text{Mg}_{0.5}\text{FeMnO}_4$  anode is a combination of diffusion-controlled intercalation and pseudocapacitance behavior.

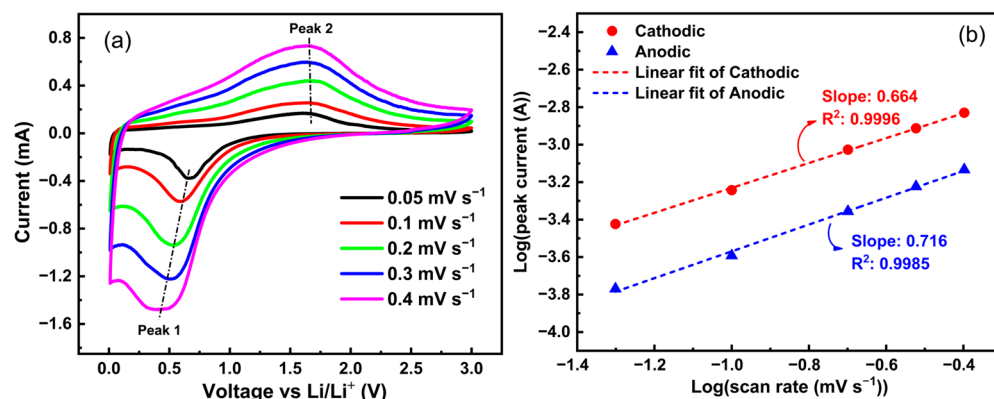


**Figure 11.** (a) Cyclic voltammetry (CV) curves of the synthesized porous  $\text{Zn}_{0.5}\text{Mg}_{0.5}\text{FeMnO}_4$  spinel oxide at scan rates of 0.05, 0.1, 0.2, 0.3, and 0.4  $\text{mV s}^{-1}$ . (b) The determination of the  $b$ -value of the synthesized porous  $\text{Zn}_{0.5}\text{Mg}_{0.5}\text{FeMnO}_4$  spinel oxide using the linear fitting of the peak currents versus scan rates.

For further study of the changes in the structure and morphology of the electrode material after cycling, and to reveal the lithium storage mechanism, ex situ XRD and SEM characterizations of the uncycled and cycled electrodes at a current density of  $0.15 \text{ A g}^{-1}$  were explored. Figure 12 shows the ex-XRD ( $20\text{--}80^\circ$ ) patterns of the synthesized  $\text{Zn}_{0.5}\text{Mg}_{0.5}\text{FeMnO}_4$  electrodes in different states: before cycling, discharged, and charged after 80 cycles. From this figure, the XRD pattern of the synthesized  $\text{Zn}_{0.5}\text{Mg}_{0.5}\text{FeMnO}_4$  electrode before cycling confirms the presence of the spinel phase, Cu foil, and the used CMC as a binder. After the discharge process, all the diffraction peaks of the  $\text{Zn}_{0.5}\text{Mg}_{0.5}\text{FeMnO}_4$  spinel phase disappear, revealing that the  $\text{Zn}_{0.5}\text{Mg}_{0.5}\text{FeMnO}_4$  spinel became an amorphous phase. Subsequently, there is no added peak observed after the charge process, revealing that it still maintains an amorphous phase under continuous lithiation/delithiation processes, which was an interesting discovery. Similar results have been obtained in several previous works that studied transition-metal-based spinels as anodes for LIBs [82,83]. According to C. Duan et al. [84], the amorphous phase formed after the first discharge is beneficial to buffer the volume change of the electrode and maintain the stability and integrity of the electrode.

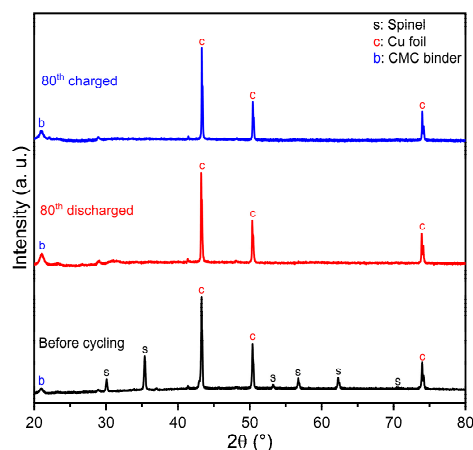


**Figure 12.** Ex-XRD patterns of the synthesized  $\text{Zn}_{0.5}\text{Mg}_{0.5}\text{FeMnO}_4$  electrodes in different states: before cycling, discharged, and charged after 80 cycles.

To demonstrate the microstructural change in the studied electrode after cycling, the SEM images of the synthesized  $\text{Zn}_{0.5}\text{Mg}_{0.5}\text{FeMnO}_4$  electrodes in different states—before cycling, discharged, and charged after 80 cycles—are displayed in Figure 13. Compared to the state before cycling, the  $\text{Zn}_{0.5}\text{Mg}_{0.5}\text{FeMnO}_4$  electrode shows significant spherical porosity constructed by 3D interconnected nanoparticles. After 80 cycles, it can be seen that the porosity of the synthesized  $\text{Zn}_{0.5}\text{Mg}_{0.5}\text{FeMnO}_4$  spinel is diminished and the surface becomes dense, whereas the size of the nanoparticles increased obviously due to the huge volume change during continuous lithiation/delithiation processes. This confirms the aggregation of  $\text{Zn}_{0.5}\text{Mg}_{0.5}\text{FeMnO}_4$  nanoparticles, which led to a reduction in the specific surface area. This reduction in the specific surface area can explain the gradual decrease and poor stability of the specific capacity during discharge/charge processes with cycling.

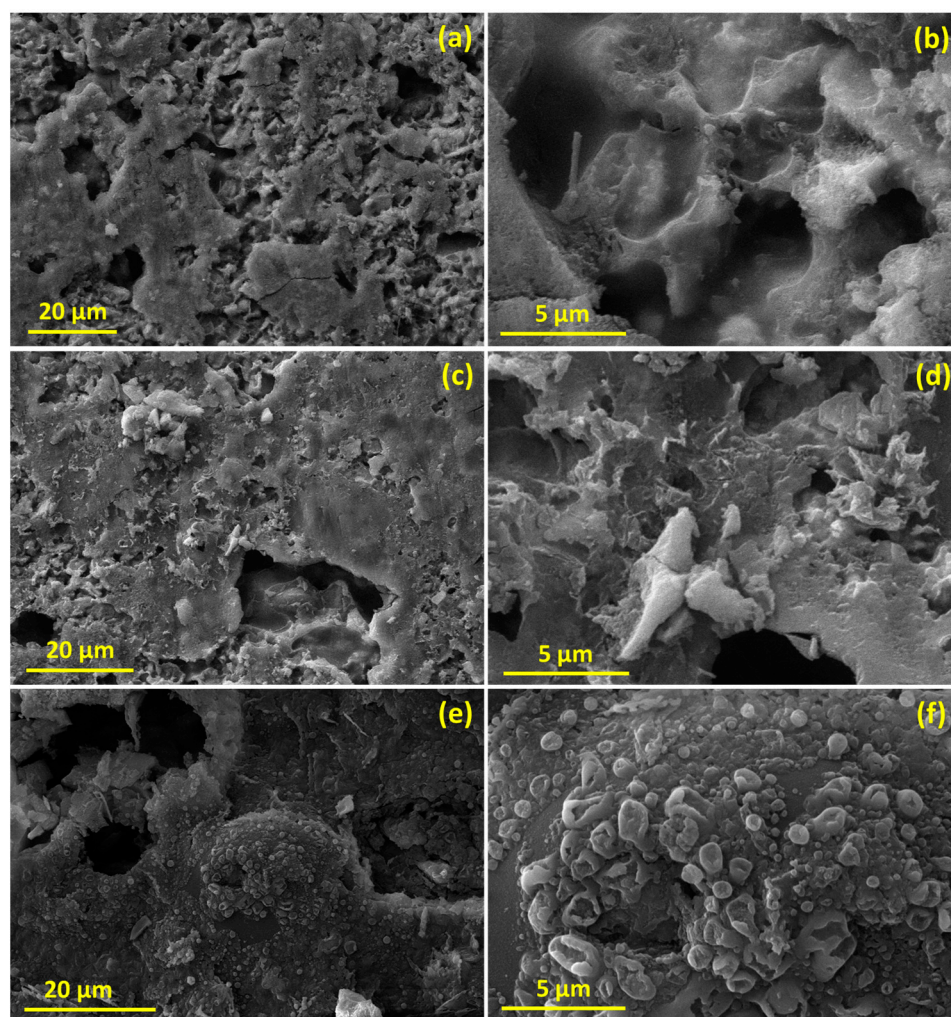


**Figure 13.** SEM images of the synthesized  $\text{Zn}_{0.5}\text{Mg}_{0.5}\text{FeMnO}_4$  electrodes (a,b) before cycling, (c,d) discharged after 80 cycles, and (e,f) charged after 80 cycles.

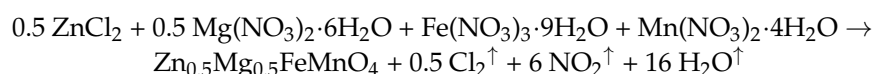
### 3. Materials and Methods

#### 3.1. Materials

Zinc chloride  $\text{ZnCl}_2$ , magnesium nitrate hexahydrate  $\text{Mg}(\text{NO}_3)_2 \cdot 6\text{H}_2\text{O}$ , iron nitrate nonahydrate  $\text{Fe}(\text{NO}_3)_3 \cdot 9\text{H}_2\text{O}$ , manganese nitrate tetrahydrate  $\text{Mn}(\text{NO}_3)_2 \cdot 4\text{H}_2\text{O}$ , and citric acid monohydrate  $\text{C}_6\text{H}_8\text{O}_7 \cdot \text{H}_2\text{O}$  of analytical grade were purchased from Sigma Aldrich. All purchased reagents were directly used as received without further purification.

### 3.2. Synthesis of the Porous $Zn_{0.5}Mg_{0.5}FeMnO_4$ Spinel

The porous  $Zn_{0.5}Mg_{0.5}FeMnO_4$  spinel oxide was synthesized using a facile sol–gel method. Initially, specific molar ratios of  $ZnCl_2$ ,  $Mg(NO_3)_2 \cdot 6H_2O$ ,  $Fe(NO_3)_3 \cdot 9H_2O$ , and  $Mn(NO_3)_2 \cdot 4H_2O$  were dissolved together in deionized water under vigorous magnetic stirring for 30 min to obtain a homogeneous solution. To this homogeneous solution, citric acid (CA) dissociated in deionized water was added at a molar ratio of  $CA/cations = 2.5$ . Then, the solution was kept on the hot plate at  $90\text{ }^\circ\text{C}$  until a viscous gel formed followed by cooling slowly down to room temperature. Subsequently, the resulting gel was dried in an oven at  $120\text{ }^\circ\text{C}$  for 12 h to obtain the xerogel powder. Finally, the as-synthesized powder was annealed in the furnace at  $700\text{ }^\circ\text{C}$  for 12 h at a heating rate of  $3\text{ }^\circ\text{C min}^{-1}$  in air to obtain the porous  $Zn_{0.5}Mg_{0.5}FeMnO_4$  spinel oxide. During this synthesis, the  $Zn_{0.5}Mg_{0.5}FeMnO_4$  spinel oxide was formed from the reagents according to the following chemical reaction:



### 3.3. Characterization Techniques

For the structural analysis and the phase identification, the synthesized porous  $Zn_{0.5}Mg_{0.5}FeMnO_4$  spinel was firstly characterized by powder X-ray diffraction (XRD, Bruker D8 Advance) with  $Cu-K\alpha$  ( $\lambda_1 = 1.54056\text{ \AA}$  and  $\lambda_2 = 1.54439\text{ \AA}$ ) radiations. The XRD analysis was carried out at room temperature over a  $2\theta$  range from  $10^\circ$  to  $80^\circ$  at a scan rate of  $0.02^\circ/s$ . The structural refinement of the prepared sample was carried out by the Rietveld method using Full-prof software (version 7.95) [85]. Thermal stability of the synthesized xerogel and calcined sample was investigated by thermogravimetric analysis (TGA) performed on a Discovery TGA analyzer in the temperature range of  $20\text{--}700\text{ }^\circ\text{C}$  at a heating rate of  $10\text{ }^\circ\text{C min}^{-1}$  under a constant air purging flow. The surface morphology and surface elemental composition of the prepared powder spinel were evaluated by employing a scanning electron microscope interconnected with an energy-dispersive X-ray spectrometer (SEM/EDX, Zeiss Evo 10). For further deep analysis of the surface morphology, a high-resolution scanning electron microscopy (HR-SEM) image was obtained on a JEOL JSM-IT500HR instrument. To obtain the Brunauer–Emmett–Teller (BET) specific surface area of the synthesized porous spinel, the nitrogen adsorption–desorption isotherm was collected at a liquid nitrogen temperature of  $77\text{ K}$  using a Micromeritics Instrument.

### 3.4. Electrochemical Measurements

To make the working electrodes of  $Zn_{0.5}Mg_{0.5}FeMnO_4$  spinel, dry powders of the synthesized spinel (active material), carbon black, and carboxymethyl cellulose (CMC) binder were mixed at a weight ratio of 80:10:10, respectively. To form a homogeneous slurry, the mixture was dispersed in ultrapure water and mixed for 2 h under vigorous magnetic stirring. Subsequently, the above slurry mixture was cast on a copper foil current collector with a thickness of  $0.1\text{ mm}$  and a mass loading of  $1\text{--}1.2\text{ mg cm}^{-2}$  using the doctor-blade technique. The loaded copper foil was dried at  $60\text{ }^\circ\text{C}$  under vacuum for 4 h to eliminate the water used as a solvent and then cut into disks of  $11\text{ mm}$  in diameter. The produced electrodes were dried at  $80\text{ }^\circ\text{C}$  under vacuum for 12 h. All the electrochemical measurements of  $Zn_{0.5}Mg_{0.5}FeMnO_4$  spinel as anode material for LIBs were performed at room temperature using CR2032 coin cells in a half-cell configuration.  $Zn_{0.5}Mg_{0.5}FeMnO_4//Li$  coin cells were assembled in an Ar (99.999%)-filled glove box (Jacomex, France,  $H_2O$  and  $O_2$  contents  $\leq 1.0\text{ ppm}$ ) with high-purity metallic lithium disks as the counter and reference electrodes, Whatman as a separator, and a solution of  $LiPF_6$  ( $2\text{ mol L}^{-1}$ ) dissolved in EMC as the electrolyte. Their electrochemical performance was examined using a BioLogic Science multi-channel battery cyler for testing cyclic voltammetry (CV), galvanostatic discharge/charge, long-term cycling, and rate capability over the  $0.01\text{--}3.00\text{ V}$  voltage range (vs.  $Li^+/Li$ ). The cyclic voltammetry (CV) data were measured at various scan rates:  $0.05, 0.10, 0.20, 0.30,$  and  $0.40\text{ mV s}^{-1}$ . The galvanostatic discharge/charge and

long-term cycling of the studied spinel were performed at a current density of  $150 \text{ mA g}^{-1}$ . Moreover, the rate capability analysis was realized at different current densities of 150, 200, 300, and  $400 \text{ mA g}^{-1}$ . The assembled coin cells were set still for 7 h before testing. In this work, the discharging and charging are considered as the lithiation and delithiation processes, respectively.

#### 4. Conclusions

In this work, the electrochemical performance of a porous  $\text{Zn}_{0.5}\text{Mg}_{0.5}\text{FeMnO}_4$  spinel oxide elaborated by a facile sol–gel route as anode material for LIBs was investigated in detail. As demonstrated by the XRD, Rietveld method, SEM, and EDX results, the product has a high-purity phase with the desired chemical composition. From the structural analysis, the formation of a single  $\text{AB}_2\text{O}_4$ -type spinel phase of the synthesized sample was confirmed. Rietveld refinement evidenced the cubic spinel with  $Fd\bar{3}m$  symmetry. Under flowing air, the synthesized porous  $\text{Zn}_{0.5}\text{Mg}_{0.5}\text{FeMnO}_4$  spinel oxide showed a good thermal stability as the temperature increased to  $700^\circ\text{C}$ . The SEM image confirmed the successful formation of porous morphology with pore sizes ranging from 2 to  $5 \mu\text{m}$ . From the HR-SEM image, the 3D interconnection of the nanosized spherical particles led to a porous morphology. According to the BET method, the specific surface area of the synthesized porous  $\text{Zn}_{0.5}\text{Mg}_{0.5}\text{FeMnO}_4$  spinel oxide was found to be  $13.54 \text{ m}^2 \text{ g}^{-1}$ . For the electrochemical performance, the  $\text{Zn}_{0.5}\text{Mg}_{0.5}\text{FeMnO}_4$  anode showed good cycling stability in its capacity during the initial 40 cycles, with a retention capacity of  $484.1 \text{ mAh g}^{-1}$  after 40 cycles at a current density of  $150 \text{ mA g}^{-1}$ , followed by a gradual decrease in the range of 40–80 cycles, which led to reaching a specific capacity close to  $300.0 \text{ mAh g}^{-1}$  after 80 cycles at a current density of  $150 \text{ mA g}^{-1}$ . Besides, the electrochemical reactions of the lithiation/delithiation processes were extracted from the CV curves. For the lithium-ion storage mechanism, a combination of diffusion-controlled intercalation and pseudocapacitance behavior was found. In general, this work is a way forward to develop inexpensive, highly efficient, and eco-friendly transition-metal oxide as a promising anode material for LIBs.

**Author Contributions:** Conceptualization, Z.C., A.L. and B.M.; methodology, Z.C. and B.M.; software, Z.C. and O.E.G.; validation, A.L., J.A. and B.M.; formal analysis, Z.C. and O.E.G.; investigation, Z.C. and B.M.; data curation, Z.C. and O.E.G.; writing—original draft preparation, Z.C.; writing—review and editing, A.L., J.A. and B.M.; visualization, O.E.G.; supervision, B.M.; project administration, J.A. and B.M. All authors have read and agreed to the published version of the manuscript.

**Funding:** This work was financed by The Energy Sustainability chair, ENSUS, founded by Mohammed VI Polytechnic University and the OCP Foundation of Morocco.

**Institutional Review Board Statement:** Not applicable.

**Informed Consent Statement:** Not applicable.

**Data Availability Statement:** Not applicable.

**Acknowledgments:** The authors would like to thank The Energy Sustainability chair, ENSUS, founded by Mohammed VI Polytechnic University and the OCP Foundation of Morocco.

**Conflicts of Interest:** The authors declare no conflict of interest.

**Sample Availability:** Samples of the  $\text{Zn}_{0.5}\text{Mg}_{0.5}\text{FeMnO}_4$  compound are available from the authors.

#### References

1. Li, L.; Song, J.; Lu, Q.; Tan, X. Synthesis of Nano-Crystalline  $\text{Sm}_{0.5}\text{Sr}_{0.5}\text{Co}(\text{Fe})\text{O}_{3-\delta}$  Perovskite Oxides by a Microwave-Assisted Sol–Gel Combustion Process. *Ceram. Int.* **2014**, *40*, 1189–1194. [[CrossRef](#)]
2. Shen, D.; Jia, M.; Li, M.; Fu, X.; Liu, Y.; Dong, W.; Yang, S. High Coulomb Efficiency Sn–Co Alloy/RGO Composite Anode Material for Li–Ion Battery with Long Cycle–Life. *Molecules* **2023**, *28*, 3923. [[CrossRef](#)]
3. Liu, G.; Jin, B.; Zhang, R.; Bao, K.; Xie, H.; Guo, J.; Wei, M.; Jiang, Q. Synthesis of  $\text{Ti}_2\text{Nb}_{10}\text{O}_{29}/\text{C}$  Composite as an Anode Material for Lithium-Ion Batteries. *Int. J. Hydrogen Energy* **2016**, *41*, 14807–14812. [[CrossRef](#)]
4. Deng, Y.; Zhang, Q.; Tang, S.; Zhang, L.; Deng, S.; Shi, Z.; Chen, G. One-Pot Synthesis of  $\text{ZnFe}_2\text{O}_4/\text{C}$  Hollow Spheres as Superior Anode Materials for Lithium Ion Batteries. *Chem. Commun.* **2011**, *47*, 6828. [[CrossRef](#)]

5. Hou, L.; Lian, L.; Zhang, L.; Pang, G.; Yuan, C.; Zhang, X. Self-Sacrifice Template Fabrication of Hierarchical Mesoporous Bi-Component-Active ZnO/ZnFe<sub>2</sub>O<sub>4</sub> Sub-Microcubes as Superior Anode Towards High-Performance Lithium-Ion Battery. *Adv. Funct. Mater.* **2015**, *25*, 238–246. [[CrossRef](#)]
6. Zhang, G.; Chen, M.; Li, C.; Wu, B.; Chen, J.; Xiang, W.; Wen, X.; Zhang, D.; Cao, G.; Li, W. Surface Spinel and Interface Oxygen Vacancies Enhanced Lithium-Rich Layered Oxides with Excellent Electrochemical Performances. *Chem. Eng. J.* **2022**, *443*, 136434. [[CrossRef](#)]
7. Meister, P.; Jia, H.; Li, J.; Kloepsch, R.; Winter, M.; Placke, T. Best Practice: Performance and Cost Evaluation of Lithium Ion Battery Active Materials with Special Emphasis on Energy Efficiency. *Chem. Mater.* **2016**, *28*, 7203–7217. [[CrossRef](#)]
8. Cheng, X.-B.; Zhang, R.; Zhao, C.-Z.; Zhang, Q. Toward Safe Lithium Metal Anode in Rechargeable Batteries: A Review. *Chem. Rev.* **2017**, *117*, 10403–10473. [[CrossRef](#)]
9. Zhang, X.; Jiang, R.; Fan, C.; Xie, D.; Li, B.; Zhang, J.; Wu, X. Engineering All-Purpose Amorphous Carbon Nanotubes with High N/O-Co-Doping Content to Bridge the Alkali-Ion Batteries and Li Metal Batteries. *Small* **2021**, *17*, 2006566. [[CrossRef](#)]
10. Zha, G.; Hu, W.; Agarwal, S.; Ouyang, C.; Hu, N.; Hou, H. High Performance Layered LiNi<sub>0.8</sub>Co<sub>0.07</sub>Fe<sub>0.03</sub>Mn<sub>0.1</sub>O<sub>2</sub> Cathode Materials for Li-Ion Battery. *Chem. Eng. J.* **2021**, *409*, 128343. [[CrossRef](#)]
11. Lim, Y.E.; Choi, W.S.; Kim, J.H.; Ahn, Y.N.; Kim, I.T. The Sn-Red P-Fe-Based Alloy Materials for Efficient Li-Ion Battery Anodes. *J. Ind. Eng. Chem.* **2023**, *121*, 299–311. [[CrossRef](#)]
12. Bae, J.-H.; Nyamaa, O.; Lee, J.-S.; Yun, S.; Woo, S.-M.; Yang, J.-H.; Kim, M.-S.; Noh, J.-P. Electrochemical Properties of the Si Thin-Film Anode Deposited on Ti-Nb-Zr Shape Memory Alloy in Li-Ion Batteries. *Electrochem. Commun.* **2022**, *140*, 107315. [[CrossRef](#)]
13. Shang, C.; Li, X.; Wei, R.; Liu, X.; Xu, S.; Zhang, J. Research Progress of Metal Oxide Glass Anode Materials for Lithium-Ion Batteries: A Review. *J. Non. Cryst. Solids* **2023**, *618*, 122547. [[CrossRef](#)]
14. Lamhani, M.; Chchiyai, Z.; Elomrani, A.; Manoun, B.; Hasnaoui, A. The Effect of Sr Substitution on the Structural and Physical Properties of Manganite Perovskites Ca<sub>1-x</sub>Sr<sub>x</sub>MnO<sub>3-δ</sub> (0 ≤ x ≤ 1). *Phys. Chem. Chem. Phys.* **2022**, *24*, 19414–19431. [[CrossRef](#)]
15. Kouchi, K.; Tayoury, M.; Chari, A.; Chchiyai, Z.; Hdidou, L.; Tamraoui, Y.; Alami, J.; Manoun, B.; Dahbi, M. Sol Gel Synthesis of Nanoparticles Ni<sub>0.5</sub>Mg<sub>0.5</sub>Fe<sub>1.7</sub>Mn<sub>0.3</sub>O<sub>4</sub> as Anode Material for Lithium-Ion Batteries. In Proceedings of the 2021 9th International Renewable and Sustainable Energy Conference (IRSEC), Tetouan, Morocco, 23–27 November 2021; IEEE: Piscataway, NJ, USA; pp. 1–5.
16. Huang, S.; Li, H.; Xu, G.; Liu, X.; Zhang, Q.; Yang, L.; Cao, J.; Wei, X. Porous N-Doped Carbon Sheets Wrapped MnO in 3D Carbon Networks as High-Performance Anode for Li-Ion Batteries. *Electrochim. Acta* **2020**, *342*, 136115. [[CrossRef](#)]
17. Chu, K.; Li, Z.; Xu, S.; Yao, G.; Xu, Y.; Niu, P.; Zheng, F. NiO Nanocrystals Encapsulated into a Nitrogen-Doped Porous Carbon Matrix as Highly Stable Li-Ion Battery Anodes. *J. Alloys Compd.* **2021**, *854*, 157264. [[CrossRef](#)]
18. Su, Y.; Liu, T.; Zhang, P.; Zheng, P. CuO Nanowire Arrays Synthesized at Room Temperature as a High-Performance Anode Material for Li/Na-Ion Batteries. *Thin Solid Films* **2019**, *690*, 137522. [[CrossRef](#)]
19. Li, Y.; Liu, S.; Lu, X.; Zhao, H.; Cui, J.; Zhang, Y.; He, W. Hydrothermal Synthesis of Carbon-Coated Mixed Crystalline Phase TiO<sub>2</sub> Nanoparticle Carbon Microsphere Composites as High Performance Anode Materials for Li-Ion Batteries. *Diam. Relat. Mater.* **2023**, *136*, 109913. [[CrossRef](#)]
20. Liu, D.; Choi, W.M. Hierarchical Hollow Urchin-like Structured MnO<sub>2</sub> Microsphere/Carbon Nanofiber Composites as Anode Materials for Li-Ion Batteries. *Curr. Appl. Phys.* **2019**, *19*, 768–774. [[CrossRef](#)]
21. Buga, M.-R.; Spinu-Zaulet, A.A.; Ungureanu, C.G.; Mitran, R.-A.; Vasile, E.; Florea, M.; Neatu, F. Carbon-Coated SiO<sub>2</sub> Composites as Promising Anode Material for Li-Ion Batteries. *Molecules* **2021**, *26*, 4531. [[CrossRef](#)]
22. Golmohammad, M.; Sazvar, A.; Maleki Shahraki, M.; Golestanifard, F. Synthesis and Characterization of Bar-like Maghemite (γ-Fe<sub>2</sub>O<sub>3</sub>) as an Anode for Li-Ion Batteries. *Ceram. Int.* **2022**, *48*, 27148–27153. [[CrossRef](#)]
23. Wen, Z.; Rong, Z.; Yin, Y.; Ren, H.; Woo Joo, S.; Huang, J. N-Doped Carbon Coated SnO<sub>2</sub> Nanospheres as Li-Ion Battery Anode with High Capacity and Good Cycling Stability. *J. Electroanal. Chem.* **2021**, *899*, 115694. [[CrossRef](#)]
24. Allen, J.L.; Crear, B.A.; Choudhury, R.; Wang, M.J.; Tran, D.T.; Ma, L.; Piccoli, P.M.; Sakamoto, J.; Wolfenstine, J. Fast Li-Ion Conduction in Spinel-Structured Solids. *Molecules* **2021**, *26*, 2625. [[CrossRef](#)] [[PubMed](#)]
25. Drozhzhin, O.A.; Shevchenko, V.A.; Bobyleva, Z.V.; Alekseeva, A.M.; Antipov, E.V. Rational Screening of High-Voltage Electrolytes and Additives for Use in LiNi<sub>0.5</sub>Mn<sub>1.5</sub>O<sub>4</sub>-Based Li-Ion Batteries. *Molecules* **2022**, *27*, 3596. [[CrossRef](#)] [[PubMed](#)]
26. Sanad, M.M.S.; Azab, A.A.; Taha, T.A. Introduced Oxygen Vacancies in Cadmium Ferrite Anode Materials via Zn<sup>2+</sup> Incorporation for High Performance Lithium-Ion Batteries. *Mater. Sci. Semicond. Process.* **2022**, *143*, 106567. [[CrossRef](#)]
27. Mazur, Ł.; Koszelow, D.; Zajusz, M.; Łapiński, M.; Bik, M.; Zając, P.; Adamczyk, A.; Rutkowski, P.; Molin, S.; Brylewski, T. Comparison of Cu<sub>1.3</sub>Mn<sub>1.7</sub>O<sub>4</sub> Spinel Doped with Ni or Fe and Synthesized via Wet Chemistry and Solid-State Reaction Methods, Designed as Potential Coating Materials for Metallic Interconnects. *J. Eur. Ceram. Soc.* **2023**, *43*, 5557–5574. [[CrossRef](#)]
28. Nyamaa, O.; Kang, G.-H.; Huh, S.-C.; Yang, J.-H.; Nam, T.-H.; Noh, J.-P. Unraveling the Mechanism and Practical Implications of the Sol-Gel Synthesis of Spinel LiMn<sub>2</sub>O<sub>4</sub> as a Cathode Material for Li-Ion Batteries: Critical Effects of Cation Distribution at the Matrix Level. *Molecules* **2023**, *28*, 3489. [[CrossRef](#)]
29. Afzia, M.; Khan, R.A.; Ismail, B.; Zaki, M.E.A.; Althagafi, T.M.; Alanazi, A.A.; Khan, A.U. Correlation between Magnetic and Dielectric Response of CoFe<sub>2</sub>O<sub>4</sub>:Li<sup>1+</sup>/Zn<sup>2+</sup> Nanopowders Having Improved Structural and Morphological Properties. *Molecules* **2023**, *28*, 2824. [[CrossRef](#)]

30. Nguyen, T.X.; Tsai, C.-C.; Patra, J.; Clemens, O.; Chang, J.-K.; Ting, J.-M. Co-Free High Entropy Spinel Oxide Anode with Controlled Morphology and Crystallinity for Outstanding Charge/Discharge Performance in Lithium-Ion Batteries. *Chem. Eng. J.* **2022**, *430*, 132658. [[CrossRef](#)]
31. Saroha, R.; Seon, Y.H.; Jin, B.; Kang, Y.C.; Kang, D.-W.; Jeong, S.M.; Cho, J.S. Self-Supported Hierarchically Porous 3D Carbon Nanofiber Network Comprising Ni/Co/NiCo<sub>2</sub>O<sub>4</sub> Nanocrystals and Hollow N-Doped C Nanocages as Sulfur Host for Highly Reversible Li-S Batteries. *Chem. Eng. J.* **2022**, *446*, 137141. [[CrossRef](#)]
32. Li, Z.; Wang, D.; Gu, A.; Wei, W.; Lv, H.; Lou, Z.; Zhou, Q. Ethylene Glycol Combustion Strategy towards 3D Mesoporous ZnCo<sub>2</sub>O<sub>4</sub> as Anodes for Li-Ion Batteries. *Solid State Ionics* **2020**, *356*, 115461. [[CrossRef](#)]
33. Chen, R.; Wen, B.; Li, H.; Xiang, M.; Su, C.; Guo, J.; Bai, W.; Sa, Z. Facile Preparation of High-Performance Spinel LiMn<sub>2-x</sub>Cu<sub>x</sub>O<sub>4</sub> Cathodes by Microwave-Induced Solution Flameless Combustion. *Vacuum* **2021**, *187*, 110077. [[CrossRef](#)]
34. Wu, S.; Su, H.-J. Electrochemical Characteristics of Partially Cobalt-Substituted LiMn<sub>2-y</sub>Co<sub>y</sub>O<sub>4</sub> Spinel Synthesized by Pechini Process. *Mater. Chem. Phys.* **2003**, *78*, 189–195. [[CrossRef](#)]
35. Qi, C.; Zhao, M.; Fang, T.; Zhu, Y.; Wang, P.; Xie, A.; Shen, Y. Multifunctional Hollow Porous Fe<sub>3</sub>O<sub>4</sub>@N-C Nanocomposites as Anodes of Lithium-Ion Battery, Adsorbents and Surface-Enhanced Raman Scattering Substrates. *Molecules* **2023**, *28*, 5183. [[CrossRef](#)] [[PubMed](#)]
36. Sankar, A.; Paramasivaganesh, K.; Parthibavarman, M.; Meganathan, K.L. ZIF-8 Derived CuFe<sub>2</sub>O<sub>4</sub> Nanoparticles: Evolution of Composition and Microstructures, and Their Electrochemical Performances as Anode for Lithium-Ion Batteries. *Inorg. Chem. Commun.* **2022**, *140*, 109424. [[CrossRef](#)]
37. Karunakaran, G.; Kundu, M.; Maduraiveeran, G.; Kolesnikov, E.; Gorshenkov, M.V.; Balasingam, S.K.; Kumari, S.; Sasidharan, M.; Kuznetsov, D. Hollow Mesoporous Heterostructures Negative Electrode Comprised of CoFe<sub>2</sub>O<sub>4</sub>@Fe<sub>3</sub>O<sub>4</sub> for next Generation Lithium Ion Batteries. *Microporous Mesoporous Mater.* **2018**, *272*, 1–7. [[CrossRef](#)]
38. Mujahid, M.; Ullah Khan, R.; Mumtaz, M.; Mubasher; Soomro, S.A.; Ullah, S. NiFe<sub>2</sub>O<sub>4</sub> Nanoparticles/MWCNTs Nanohybrid as Anode Material for Lithium-Ion Battery. *Ceram. Int.* **2019**, *45*, 8486–8493. [[CrossRef](#)]
39. Du, F.-H.; Li, S.-Q.; Yan, Y.; Lu, X.-M.; Guo, C.; Ji, Z.; Hu, P.; Shen, X. Facile Fabrication of Fe<sub>0.8</sub>Mn<sub>1.2</sub>O<sub>3</sub> with Various Nanostructures for High-Performance Lithium-Ion Batteries. *Chem. Eng. J.* **2022**, *427*, 131697. [[CrossRef](#)]
40. Pan, Y.; Zhang, Y.; Wei, X.; Yuan, C.; Yin, J.; Cao, D.; Wang, G. MgFe<sub>2</sub>O<sub>4</sub> Nanoparticles as Anode Materials for Lithium-Ion Batteries. *Electrochim. Acta* **2013**, *109*, 89–94. [[CrossRef](#)]
41. Zhang, Z.; Wang, Y.; Tan, Q.; Zhong, Z.; Su, F. Facile Solvothermal Synthesis of Mesoporous Manganese Ferrite (MnFe<sub>2</sub>O<sub>4</sub>) Microspheres as Anode Materials for Lithium-Ion Batteries. *J. Colloid Interface Sci.* **2013**, *398*, 185–192. [[CrossRef](#)]
42. Guo, X.; Lu, X.; Fang, X.; Mao, Y.; Wang, Z.; Chen, L.; Xu, X.; Yang, H.; Liu, Y. Lithium Storage in Hollow Spherical ZnFe<sub>2</sub>O<sub>4</sub> as Anode Materials for Lithium Ion Batteries. *Electrochem. Commun.* **2010**, *12*, 847–850. [[CrossRef](#)]
43. Wu, W.; Wei, Y.; Chen, H.; Wei, K.; Li, Z.; He, J.; Deng, L.; Yao, L.; Yang, H. In-Situ Encapsulation of  $\alpha$ -Fe<sub>2</sub>O<sub>3</sub> Nanoparticles into ZnFe<sub>2</sub>O<sub>4</sub> Micro-Sized Capsules as High-Performance Lithium-Ion Battery Anodes. *J. Mater. Sci. Technol.* **2021**, *75*, 110–117. [[CrossRef](#)]
44. Zhao, T.; Zheng, Y.; Meng, Y.; Huang, X.; Chen, S.; Chang, L.; Shen, J. ZnFe<sub>2</sub>O<sub>4</sub> Nanoparticles Embedded Dispersedly inside 3D Porous Carbon Framework as Advanced Anode Materials of Li-Ion Batteries. *J. Alloys Compd.* **2022**, *913*, 165279. [[CrossRef](#)]
45. Qu, Y.; Zhang, D.; Wang, X.; Qiu, H.; Zhang, T.; Zhang, M.; Tian, G.; Yue, H.; Feng, S.; Chen, G. Porous ZnFe<sub>2</sub>O<sub>4</sub> Nanospheres as Anode Materials for Li-Ion Battery with High Performance. *J. Alloys Compd.* **2017**, *721*, 697–704. [[CrossRef](#)]
46. Wang, J.; Yang, G.; Wang, L.; Yan, W. Fabrication of the ZnFe<sub>2</sub>O<sub>4</sub> Fiber-in-Tube and Tubular Mesoporous Nanostructures via Single-Spinneret Electrospinning: Characterization, Mechanism and Performance as Anodes for Li-Ion Batteries. *Electrochim. Acta* **2016**, *222*, 1176–1185. [[CrossRef](#)]
47. Chen, W.; Du, R.; Liang, H.; Zhou, Z.; Shao, L.; Shu, J.; Wang, Z. Lithium Storage Behavior of Manganese Based Complex Spinel Titanate as Anode Material for Li-Ion Batteries. *J. Power Sources* **2014**, *272*, 622–628. [[CrossRef](#)]
48. Liang, Z.; Tu, H.; Kong, Z.; Yao, X.; Xu, D.; Liu, S.; Shao, Y.; Wu, Y.; Hao, X. Urchin like Inverse Spinel Manganese Doped NiCo<sub>2</sub>O<sub>4</sub> Microspheres as High Performances Anode for Lithium-Ion Batteries. *J. Colloid Interface Sci.* **2022**, *616*, 509–519. [[CrossRef](#)]
49. Cai, K.; Luo, S.H.; Cong, J.; Li, K.; Yan, S.X.; Hou, P.Q.; Wang, Q.; Zhang, Y.; Liu, X.; Lei, X.; et al. Facile Microwave-Assisted Hydrothermal Synthesis and Improved Electrochemical Performance of Micro Rhombus ZnMn<sub>2</sub>O<sub>4</sub> Anodes for Li-Ion Batteries. *J. Electroanal. Chem.* **2022**, *912*, 116237. [[CrossRef](#)]
50. Wang, Z.; Ai, L.; Ding, J.; Zhu, P.; Zhuang, J.; Zhao, J.; Li, B.; Yu, F.; Duan, X. MgMn<sub>2</sub>O<sub>4</sub> Anode Materials for Lithium-Ion Batteries: Synthesis and Cationic Distribution Study. *Vacuum* **2022**, *201*, 111075. [[CrossRef](#)]
51. Dong, L.; Wang, Z.; Li, Y.; Jin, C.; Dong, F.; Zhao, W.; Qin, C.; Wang, Z. Spinel-Structured, Multi-Component Transition Metal Oxide (Ni,Co,Mn)Fe<sub>2</sub>O<sub>4-x</sub> as Long-Life Lithium-Ion Battery Anode Material. *Batteries* **2023**, *9*, 54. [[CrossRef](#)]
52. Tian, K.-H.; Duan, C.-Q.; Ma, Q.; Li, X.-L.; Wang, Z.-Y.; Sun, H.-Y.; Luo, S.-H.; Wang, D.; Liu, Y.-G. High-Entropy Chemistry Stabilizing Spinel Oxide (CoNiZnXMnLi)<sub>3</sub>O<sub>4</sub> (X = Fe, Cr) for High-Performance Anode of Li-Ion Batteries. *Rare Met.* **2022**, *41*, 1265–1275. [[CrossRef](#)]
53. Liu, Y.; Russo, P.A.; Montoro, L.A.; Pinna, N. Recent Developments in Nb-based Oxides with Crystallographic Shear Structures as Anode Materials for High-rate Lithium-ion Energy Storage. *Batter. Energy* **2023**, *2*, 20220037. [[CrossRef](#)]
54. Yu, Y.; Li, M.; Li, Q.; Zhang, J.; Sun, M.; Qi, W.; Li, J. Core-Shell MgFe<sub>2</sub>O<sub>4</sub>@C Nano-Composites Derived via Thermal Decomposition-Reduction Dual Strategy for Superior Lithium Storage. *J. Alloys Compd.* **2020**, *834*, 155207. [[CrossRef](#)]

55. Chchiyai, Z.; El Bachraoui, F.; Tamraoui, Y.; Bih, L.; Faik, A.; Alami, J.; Manoun, B. Design and Characterization of Novel Manganite Perovskites  $Ba_{1-x}Bi_xTi_{1-x}Mn_xO_3$  ( $0 \leq x \leq 0.2$ ). *Ceram. Int.* **2020**, *46*, 26911–26922. [[CrossRef](#)]
56. Chchiyai, Z.; El Bachraoui, F.; Tamraoui, Y.; Haily, E.M.; Bih, L.; Lahmar, A.; Alami, J.; Manoun, B. Design, Structural Evolution, Optical, Electrical and Dielectric Properties of Perovskite Ceramics  $Ba_{1-x}Bi_xTi_{1-x}Fe_xO_3$  ( $0 \leq x \leq 0.8$ ). *Mater. Chem. Phys.* **2021**, *273*, 125096. [[CrossRef](#)]
57. Chchiyai, Z.; El Bachraoui, F.; Tamraoui, Y.; Bih, L.; Lahmar, A.; Faik, A.; Alami, J.; Manoun, B. Synthesis, Structural Refinement and Physical Properties of Novel Perovskite Ceramics  $Ba_{1-x}Bi_xTi_{1-x}Mn_xO_3$  ( $x = 0.3$  and  $0.4$ ). *Mater. Chem. Phys.* **2021**, *262*, 124302. [[CrossRef](#)]
58. Chchiyai, Z.; El Bachraoui, F.; Tamraoui, Y.; Mehdi Haily, E.; Bih, L.; Lahmar, A.; El Marssi, M.; Alami, J.; Manoun, B. Effect of Cobalt Doping on the Crystal Structure, Magnetic, Dielectric, Electrical and Optical Properties of  $PbTi_{1-x}Co_xO_{3-\delta}$  Perovskite Materials. *J. Alloys Compd.* **2022**, *927*, 166979. [[CrossRef](#)]
59. El Bachraoui, F.; Chchiyai, Z.; Tamraoui, Y.; Louihi, S.; Alami, J.; Manoun, B. Effect of the Composition and Structure on the Optical Properties of  $Ba_{1-x}La_xTi_{1-x}Fe_xO_3$  ( $0 \leq x \leq 1$ ) Solid Solution: Correlation Study Using Rietveld Refinement. *Mater. Charact.* **2021**, *175*, 111058. [[CrossRef](#)]
60. El Bachraoui, F.; Chchiyai, Z.; Tamraoui, Y.; Louihi, S.; Alami, J.; Manoun, B.; El Moussaoui, H.; Alami, J.; Manoun, B. Optical and Magnetic Properties of Perovskite Materials:  $Ba_{0.3}La_{0.7}Ti_{0.3}Fe_{0.7}O_3$  and  $Ba_{0.1}La_{0.9}Ti_{0.1}Fe_{0.9}O_3$ . *J. Rare Earths* **2022**, *40*, 652–659. [[CrossRef](#)]
61. Placke, T.; Siozios, V.; Schmitz, R.; Lux, S.F.; Bieker, P.; Colle, C.; Meyer, H.-W.; Passerini, S.; Winter, M. Influence of Graphite Surface Modifications on the Ratio of Basal Plane to “Non-Basal Plane” Surface Area and on the Anode Performance in Lithium Ion Batteries. *J. Power Sources* **2012**, *200*, 83–91. [[CrossRef](#)]
62. Chchiyai, Z.; Hdidou, L.; Tayoury, M.; Chari, A.; Tamraoui, Y.; Alami, J.; Dahbi, M.; Manoun, B. Synthesis and Electrochemical Properties of Mn-Doped Porous  $Mg_{0.9}Zn_{0.1}Fe_{2-x}Mn_xO_4$  ( $0 \leq x \leq 1.25$ ) Spinel Oxides as Anode Materials for Lithium-Ion Batteries. *J. Alloys Compd.* **2023**, *935*, 167997. [[CrossRef](#)]
63. Zhu, S.; Li, J.; Deng, X.; He, C.; Liu, E.; He, F.; Shi, C.; Zhao, N. Ultrathin-Nanosheet-Induced Synthesis of 3D Transition Metal Oxides Networks for Lithium Ion Battery Anodes. *Adv. Funct. Mater.* **2017**, *27*, 1605017. [[CrossRef](#)]
64. Tian, L.; Zou, H.; Fu, J.; Yang, X.; Wang, Y.; Guo, H.; Fu, X.; Liang, C.; Wu, M.; Shen, P.K.; et al. Topotactic Conversion Route to Mesoporous Quasi-Single-Crystalline  $Co_3O_4$  Nanobelts with Optimizable Electrochemical Performance. *Adv. Funct. Mater.* **2010**, *20*, 617–623. [[CrossRef](#)]
65. Wang, Z.; Fei, P.; Xiong, H.; Qin, C.; Zhao, W.; Liu, X.  $CoFe_2O_4$  Nanoplates Synthesized by Dealloying Method as High Performance Li-Ion Battery Anodes. *Electrochim. Acta* **2017**, *252*, 295–305. [[CrossRef](#)]
66. Ren, Y.; Li, X.; Wang, Y.; Gu, S.; Yang, C.; Gao, T.; Cao, P.; Zhou, G. Preparation of Yolk-Double Shell  $Mn_{0.5}Zn_{0.5}Co_2O_4/C$  Nanomaterials as Anodes for High-Performance Lithium-Ion Batteries. *Appl. Mater. Today* **2022**, *27*, 101452. [[CrossRef](#)]
67. Xiao, B.; Wu, G.; Wang, T.; Wei, Z.; Sui, Y.; Shen, B.; Qi, J.; Wei, F.; Zheng, J. High-Entropy Oxides as Advanced Anode Materials for Long-Life Lithium-Ion Batteries. *Nano Energy* **2022**, *95*, 106962. [[CrossRef](#)]
68. Guan, P.; Zhou, L.; Yu, Z.; Sun, Y.; Liu, Y.; Wu, F.; Jiang, Y.; Chu, D. Recent Progress of Surface Coating on Cathode Materials for High-Performance Lithium-Ion Batteries. *J. Energy Chem.* **2020**, *43*, 220–235. [[CrossRef](#)]
69. Jiang, L.; Gao, W.; Jin, B.; Li, H.; Li, S.; Zhu, G.; Jiang, Q.  $ZnFe_2O_4/MoS_2/RGO$  Composite as an Anode for Rechargeable Lithium-Ion Batteries. *J. Electroanal. Chem.* **2018**, *823*, 407–415. [[CrossRef](#)]
70. Liu, W.; Gao, R.; Yin, Y.; Cui, Y.; Yue, H.; Dong, H.; Yang, S. 3D Hierarchical Porous N-Doped Carbon Nanosheets/ $MgFe_2O_4$  Composite as Anode Material with Excellent Cycling Stability and Rate Performance. *Scr. Mater.* **2020**, *189*, 36–41. [[CrossRef](#)]
71. Yin, Y.; Huo, N.; Liu, W.; Shi, Z.; Wang, Q.; Ding, Y.; Zhang, J.; Yang, S. Hollow Spheres of  $MgFe_2O_4$  as Anode Material for Lithium-Ion Batteries. *Scr. Mater.* **2016**, *110*, 92–95. [[CrossRef](#)]
72. Rai, A.K.; Thi, T.V.; Gim, J.; Kim, J. Combustion Synthesis of  $MgFe_2O_4$ /Graphene Nanocomposite as a High-Performance Negative Electrode for Lithium Ion Batteries. *Mater. Charact.* **2014**, *95*, 259–265. [[CrossRef](#)]
73. Jin, R.; Liu, J.; Qiu, H.; Xu, C.; Weng, L.; Liu, C.; Zeng, Y. Synthesis of Porous Nanosheet-Assembled  $ZnFe_2O_4$ @polypyrrole Yolk-Shell Microspheres as Anode Materials for High-Rate Lithium-Ion Batteries. *J. Electroanal. Chem.* **2020**, *863*, 114038. [[CrossRef](#)]
74. Zhang, Y.; Chen, S.; Meng, Y.; Chang, L.; Huang, X.; Zheng, Y.; Shen, J.; Zhao, T. CNTs Boosting Superior Cycling Stability of  $ZnFe_2O_4/C$  Nanoparticles as High-Capacity Anode Materials of Li-Ion Batteries. *J. Alloys Compd.* **2022**, *912*, 165135. [[CrossRef](#)]
75. Cai, K.; Luo, S.; Cong, J.; Li, K.; Yan, S.; Hou, P.; Song, Y.; Wang, Q.; Zhang, Y.; Liu, X.; et al. Sol-Gel Synthesis of Nano Block-like  $ZnMn_2O_4$  Using Citric Acid Complexing Agent and Electrochemical Performance as Anode for Lithium-Ion Batteries. *J. Alloys Compd.* **2022**, *909*, 164882. [[CrossRef](#)]
76. Dun, C.; Ji, X.; Xi, Y.; Yao, L.; Zhang, X.; Wang, Q.; Wu, H. Effect of N-Doped Carbon Layer on the Electrochemical Performance of  $CoFe_2O_4$  Anode Materials in Lithium-Ion Batteries Synthesized from Spent  $LiCoO_2$  Batteries. *J. Alloys Compd.* **2022**, *908*, 164661. [[CrossRef](#)]
77. Min, X.; Zhang, Y.; Yu, M.; Wang, Y.; Yuan, A.; Xu, J. A Hierarchical Dual-Carbon Supported  $ZnMn_2O_4/C$  Composite as an Anode Material for Li-Ion Batteries. *J. Alloys Compd.* **2021**, *877*, 160242. [[CrossRef](#)]
78. Zou, L.; Kang, F.; Li, X.; Zheng, Y.-P.; Shen, W.; Zhang, J. Investigations on the Modified Natural Graphite as Anode Materials in Lithium Ion Battery. *J. Phys. Chem. Solids* **2008**, *69*, 1265–1271. [[CrossRef](#)]

79. Liu, T.; Li, L.; Yao, T.; Li, Y.; Zhu, L.; Li, F.; Han, X.; Cheng, Y.; Wang, H. Integrating Amorphous Vanadium Oxide into Carbon Nanofibers via Electrospinning as High-Performance Anodes for Alkaline Ion ( $\text{Li}^+/\text{Na}^+/\text{K}^+$ ) Batteries. *Electrochim. Acta* **2021**, *369*, 137711. [[CrossRef](#)]
80. Wei, J.-L.; Wang, Z.-Y.; Sun, Y.-H.; Zhang, G.-L.; Guan, D.-C.; Nan, J.-M. The Kinetics Investigation of Nitrogen/Sulfur Co-Doped Reduced Graphene Oxide@spinel  $\text{SnFe}_2\text{O}_4/\text{Sn}_{0.205}\text{Fe}_{1.727}\text{O}_3$  as High Performance Anode for Lithium-Ion Batteries and Its Application in Full Cells. *Electrochim. Acta* **2021**, *375*, 138026. [[CrossRef](#)]
81. Yao, J.; Zhang, Y.; Yan, J.; Bin, H.; Li, Y.; Xiao, S. Nanoparticles-Constructed Spinel  $\text{ZnFe}_2\text{O}_4$  Anode Material with Superior Lithium Storage Performance Boosted by Pseudocapacitance. *Mater. Res. Bull.* **2018**, *104*, 188–193. [[CrossRef](#)]
82. Mei, C.; Hou, S.; Liu, M.; Guo, Y.; Liu, T.; Li, J.; Fu, W.; Wang, L.; Zhao, L. MOF Derived  $\text{ZnFe}_2\text{O}_4$  Nanoparticles Scattered in Hollow Octahedra Carbon Skeleton for Advanced Lithium-Ion Batteries. *Appl. Surf. Sci.* **2021**, *541*, 148475. [[CrossRef](#)]
83. Oh, S.M.; Kim, I.Y.; Adpakpang, K.; Hwang, S.-J. The Beneficial Effect of Nanocrystalline and Amorphous Nature on the Anode Performance of Manganese Oxide for Lithium Ion Batteries. *Electrochim. Acta* **2015**, *174*, 391–399. [[CrossRef](#)]
84. Duan, C.; Tian, K.; Li, X.; Wang, D.; Sun, H.; Zheng, R.; Wang, Z.; Liu, Y. New Spinel High-Entropy Oxides ( $\text{FeCoNiCrMnXLi}$ ) $_3\text{O}_4$  ( $X = \text{Cu, Mg, Zn}$ ) as the Anode Material for Lithium-Ion Batteries. *Ceram. Int.* **2021**, *47*, 32025–32032. [[CrossRef](#)]
85. Lamhani, M.; Chchiyai, Z.; Elomrani, A.; Manoun, B.; Hasnaoui, A. Enhanced Photocatalytic Water Splitting of  $\text{SrTiO}_3$  Perovskite through Cobalt Doping: Experimental and Theoretical DFT Understanding. *Inorg. Chem.* **2023**, *62*, 13405–13418. [[CrossRef](#)] [[PubMed](#)]

**Disclaimer/Publisher’s Note:** The statements, opinions and data contained in all publications are solely those of the individual author(s) and contributor(s) and not of MDPI and/or the editor(s). MDPI and/or the editor(s) disclaim responsibility for any injury to people or property resulting from any ideas, methods, instructions or products referred to in the content.